

Electronic Properties of Silver–Bismuth Iodide Rudorffite Nanoplatelets

Danijela Danilović, Aleksandar R. Milosavljević,* Pitambar Sapkota, Radovan Dojčilović, Dragana Tošić, Nenad Vukmirović, Milan Jocić, Vladimir Djoković, Sylwia Ptasińska, and Dušan K. Božanić*



Cite This: *J. Phys. Chem. C* 2022, 126, 13739–13747



Read Online

ACCESS |



Metrics & More

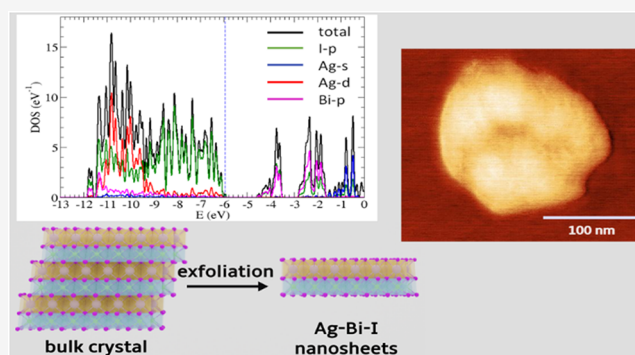


Article Recommendations



Supporting Information

ABSTRACT: Silver–bismuth iodide (Ag–Bi–I) rudorffites are chemically stable and non-toxic materials that can act as a possible lead-free replacement for methylammonium lead halides in optoelectronic applications. We report on a simple route for fabricating Ag–Bi–I colloidal nanoplatelets approximately 160 nm in lateral dimensions and 1–8 nm in thickness via exfoliation of Ag–Bi–I rudorffite powders in acetonitrile. The valence band electronic structure of isolated Ag–Bi–I nanoplatelets was investigated using synchrotron radiation to perform X-ray aerosol photoelectron spectroscopy (XAPS). The ionization energy of the material was found to be 6.1 ± 0.2 eV with respect to the vacuum level. UV–vis absorption and photoluminescence spectroscopies of the Ag–Bi–I colloids showed that the optical properties of the nanoplatelets originate from I 5p to Bi 6p and I 5p to I 5p transitions, which is further confirmed by density functional theory (DFT) calculations. Finally, calculations based on the DFT and $\mathbf{k} \cdot \mathbf{p}$ theoretical methods showed that the quantum confinement effect is very weak in the system studied.



cell absorber materials. Compared to tin-, germanium-, and antimony-based materials, bismuth-based halide perovskites appear to be the most chemically stable and the least toxic. Incorporating an Ag^+ or Cu^+ cation in the bismuth–halide lattice can lead to the formation of a new type of material with edge-shared $[\text{AX}_6]$ and $[\text{BiX}_6]$ octahedra ($A = \text{Ag}, \text{Cu}, X = \text{I}, \text{Br}$) named rudorffites.¹⁵ These metal halides may appear in many compositions that vary depending on the number of occupied sites in the cation sublattice. Several methods for fabricating silver–bismuth iodide (Ag–Bi–I) have been proposed.^{15–22} Most of these procedures were oriented toward the synthesis of bulk material. For example, Ag–Bi–I powders were produced by heating a mixture of the precursor powders at temperatures above 600 °C under vacuum,^{15,18,23} while the thin films can be fabricated via spin-coating or dynamic hot-casting of precursor solutions in organic solvents.^{16,21,24–26} In our previous study, we fabricated Ag_3BiI_6 spherical nanoparticles in the form of aerosols and investigated their

INTRODUCTION

Hybrid perovskite materials have attracted extensive research interest in recent years as they exhibit optical and semi-conducting properties favorable for the fabrication of optoelectronic devices such as solar cells, light-emitting diodes, and photodetectors.^{1–5} Among them, lead-based halide perovskites are the most studied systems since their application as absorbers in solar cells has resulted in the highest value of power conversion efficiency (PCE) of 25%.^{6,7} The exceptional performance of this type of material arises from its large absorption coefficient, low effective masses, and high mobility of charge carriers. It has been proposed that these properties originate mainly from the partially oxidized Pb^{2+} state with $6s^2 6p^0$ configuration.⁸ However, lead-based perovskite materials are unstable and easily degrade after exposure to high temperatures, electromagnetic radiation, moisture, and oxygen.^{9–12} Our previous study also showed that low-energy electrons can affect the structural and chemical properties of methylammonium lead iodide (MAPbI_3).¹³ Furthermore, lead toxicity is a serious predicament for large-scale applications.¹⁴ Thus, continuous research efforts are seeking to develop more stable and less toxic perovskite materials.

Transition metal cations, such as Bi^{3+} , Sn^{2+} , Ge^{2+} , and Sb^{3+} , also have stable, partially oxidized states, with the same $ns^2 np^0$ configuration as the lead ion. Consequently, these elements could act as suitable replacements for lead in emergent solar

Received: May 9, 2022
Revised: July 28, 2022
Published: August 9, 2022



electronic properties via synchrotron radiation X-ray aerosol photoelectron spectroscopy (XASP).²⁷

The band structure of 2D perovskite materials may depend on the size of the particles and structural modification induced by various factors.^{28–37} For example, Kanatzidis and co-workers²⁸ used organic spacer cations to create separation between adjacent layers in Ag–Bi–I particles. It was shown that the optical properties depended on the type of spacer cations used, i.e., the changes in the distances between the layers. Also, previous studies on layered semiconducting colloidal nanoparticles showed a strong effect of size reduction on their optical properties due to the confinement effect,^{38–41} which initiated the same type of research in layered perovskite nanomaterials. It was observed that Pb- and Sn-based nanoplatelets also display a strong quantum confinement effect with optical properties that depend on the particle thickness, i.e., the number of layers.^{29–33} Conversely, in the most-studied 2D lead-free systems $\text{Cs}_2\text{AgBiX}_6$ ($X = \text{Cl, Br, or I}$), the quantum confinement is rather weak.^{34,36,42} Pal et al.³⁷ also showed that $\text{Rb}_3\text{Bi}_2\text{I}_9$ 2D colloidal nanoparticles have the same band structure characteristics as their bulk counterparts.

In this work, we present a simple method for the preparation of colloidal 2D layered Ag–Bi–I ruddorffite nanostructures based on the exfoliation of Ag–Bi–I powders. The study focused on the optical properties and valence band electronic structure of the resulting nanoplatelets. The valence band structure of isolated Ag–Bi–I nanoplatelets was studied using synchrotron radiation XASP. Obtained electronic spectra were discussed and interpreted with the results from density functional theory calculations.

EXPERIMENTAL SECTION

Materials. Bismuth(III) iodide (BiI_3 , purity: 99%), silver iodide (AgI , purity: 99%), and sodium citrate tribasic dihydrate ($\text{C}_6\text{H}_5\text{Na}_3\text{O}_7 \cdot 2\text{H}_2\text{O}$) were purchased from Sigma Aldrich and used as received. Dimethyl sulfoxide (DMSO) and acetonitrile were used as solvents.

Synthesis. Ag–Bi–I nanopowder was prepared from 234 mg of AgI and 295 mg of BiI_3 powders (molar ratio of $\text{AgI}/\text{BiI}_3 = 2:1$) mixed and ground with a mortar until the mixture became light gray. The resulting powder was dissolved in 50 mL of DMSO (0.01 M). Subsequently, 10 mL of sodium citrate (0.3 M DMSO solution) was added to the solution as a stabilizing agent. The solution was stirred for 15 min, cast in a Petri dish, and heated to 120 °C in a vacuum oven to evaporate the solvent. The prepared nanopowders were characterized either in the dry state or dispersed in acetonitrile (0.6 mg/mL) to obtain the colloids. Photographs of the Ag–Bi–I powder and the Ag–Bi–I colloid are shown in Supporting Information Figure S1. For comparison with Ag–Bi–I, BiI_3 nanopowders and colloids were fabricated using the same procedure.

Characterization. X-ray diffraction (XRD) measurements of the samples deposited on an oriented Si wafer were performed using a Rigaku SmartLab system using $\text{Cu K}\alpha$ radiation (1.5406 Å, 30 mA, 40 kV) and operated in the 2θ range from 10 to 50°.

Scanning electron microscopy (SEM) analyses of powdered samples were performed with a JEOL JSM-6390 LV instrument using a 30 kV acceleration voltage. Before analysis, the samples were deposited onto an adhesive carbon tape and coated with a thin gold layer. Transmission electron microscopy (TEM) was carried out with a JEOL JEM-1400

operating at 120 kV. For the analyses, the colloidal samples were deposited onto a carbon-coated copper grid with 300 mesh and dried in vacuum.

Surface topography investigations were performed using a Quesant atomic force microscope (AFM). Colloids were deposited on freshly cleaved mica substrates by spin-coating (3500 rpm, 1 min) and investigated immediately. Measurements were made in AFM tapping mode at room temperature, using standard silicon probes Q-WM300 (force constant 40 N/m).

The UV–vis diffuse reflectance and absorption spectra of the nanopowders and dispersed colloid samples were measured with a Shimadzu UV-2600 (Shimadzu Corporation, Japan) spectrophotometer equipped with an integrating sphere (ISR-2600 Plus) over the 220–800 nm range. Photoluminescence spectra (PL) of the colloidal samples were recorded with a PerkinElmer LS45 fluorescence spectrophotometer.

Surface X-ray photoelectron spectroscopy (XPS) measurements were carried out on an ambient pressure SPECS Surface Nano Analysis GmbH X-ray photoelectron spectrometer with a monochromatic $\text{Al K}\alpha$ X-ray source (1486.6 eV). For the analysis, the acetonitrile dispersions were deposited onto a glass substrate following the procedure described in the literature by Sansom et al.²³ High-resolution spectra were recorded with a pass energy of 20 eV, which gave a full width at half-maximum of ~0.5 eV for the $\text{Au } 4f_{7/2}$ peak. The binding energy was calibrated with respect to the Fermi level by adjusting the position of the adventitious C 1s peak to 284.8 eV.²³

X-ray aerosol photoelectron spectroscopy (XAPS) was performed at the PLEIADES beamline of the SOLEIL synchrotron using the Multi-Purpose Source Chamber (MPSC) and the Scienta hemispherical electron analyzer. A detailed description of the experimental setup is provided in our previous study.²⁷ For these measurements, the Ag–Bi–I aerosols were generated from acetonitrile dispersions of Ag–Bi–I nanoparticles using a TSI 3076 atomizer. Carried by 2.5 bar of Ar gas, the aerosols were transported through a metallic tube, heated to a temperature of ~80 °C, and then cooled to 0 °C via a cold trap to remove excess acetonitrile. Subsequently, the free aerosols were introduced through a pressure-limiting orifice (250 μm in diameter) into an aerodynamic lens system and placed inside the differentially pumped stage of the MPSC. The aerodynamic lens focused the nanoparticle beam into the high-vacuum interaction region of the photoelectron spectrometer through a skimmer (1.5 mm diameter). The particle beam was ionized with 100 eV monochromatic synchrotron radiation. Gas-phase XPS spectra were recorded using a wide-angle-lens VG-Scienta R4000 electron energy analyzer. The overall resolution of the valence electron spectra was about 170 meV. Spectra were calibrated relative to the vacuum level using the binding energy of $3p_{3/2}$ Ar carrier gas at 15.76 eV^{1,43} with an overall uncertainty of less than 0.2 eV.

Calculation Methods. *Density Functional Theory Calculations with the PBE Functional.* Density functional theory (DFT) calculations were performed by modeling the exchange-correlation functional using the Perdew–Burke–Ernzerhof (PBE) generalized gradient approximation (GGA).⁴⁴ Norm-conserving fully relativistic pseudopotentials^{45,46} were used to model the effect of core electrons, and the effects of spin-orbit interaction were fully included. A Quantum Espresso code,^{47,48} which is based on the representation of wave functions in the basis of plane waves,

was used to perform these calculations. The kinetic energy cutoff for the plane-wave representation of wave functions was 50 Ry. Relaxation of lattice parameters and atomic coordinates were performed until the atomic forces were smaller than 10^{-3} Ry/bohr.

Density Functional Theory Calculation with the Hybrid PBE0 Functional. Since local and semilocal functionals in DFT (such as the PBE functional) do not result in accurate values of the band gap,⁴⁹ we also performed the calculation of bulk band structure using the hybrid PBE0 functional.^{50,51} This functional modeled the correlation energy as the PBE correlation energy, while the exchange energy was modeled as the sum of three-fourths of the PBE exchange energy and one-fourth of the Hartree–Fock exchange energy. It is known that the calculations with this functional yield band gap values that correlate significantly better with experimental band gaps of semiconducting materials than those carried out with the PBE functional (see for example refs 52 and 53). However, calculations based on the PBE0 functional are computationally significantly more demanding since they also request calculations of the Hartree–Fock exchange energy. For this reason, we used this functional only to perform bulk band structure calculations of a given bulk atomic structure. The calculation was performed using the Quantum Espresso code, where the adaptively compressed exchange operator approach for calculating exchange energy⁵⁴ is implemented.

$k \cdot p$ Calculations of the Electronic Structure. To calculate larger nanoplatelets (quantum wells), we constructed the $k \cdot p$ Hamiltonian following the approach presented in ref 55, where its parameters are determined by ab initio calculations (using either DFT/PBE or the hybrid PBE0 functional methods) of bulk material. $k \cdot p$ calculations are numerically very cheap and can therefore easily be applied to larger nanoplatelets for which DFT/PBE calculation is computationally very demanding and hybrid functional calculation is practically impossible to perform. Additional details related to $k \cdot p$ calculations are presented in the Supporting Information.

Determination of Absolute Positions of Bulk Energy Levels with Respect to Vacuum. DFT calculations with plane-wave basis and periodic boundary conditions do not yield the absolute value of the position of the energy levels with respect to vacuum. These positions were determined by performing the calculation of the interface of the material slab with vacuum as described in more detail in the Supporting Information. All the energies that we subsequently report are with vacuum as the zero energy.

RESULTS AND DISCUSSION

Characterization of the Ag–Bi–I Nanoplatelets. The results of the X-ray diffraction measurements of the Ag–Bi–I powders are presented in Figure 1a. The XRD pattern of the sample shows diffraction maxima at 2θ angles of 12.7, 23.9, 25.1, 25.6, 29.2, 32.0, 41.4, 42.2, and 43.5°, which correspond to the CdCl₂-type rhombohedral structure of a silver-rich Ag–Bi–I rudorffite system.^{15,19,56} In addition, low-intensity peaks at 22.3, 23.7, 39.2, and 46.3° indicate a small contribution of the γ -AgI phase.²⁰ Similar diffraction patterns were observed in various other types of Ag–Bi–I structures, for example, Ag₃BiI₆ nanoparticles produced in the gas phase from iodide precursors,²⁷ Ag–Bi–I nanoparticles fabricated from nitrate salts,⁵⁷ Ag–Bi–I thin films produced by the dynamic hot-casting method,²¹ and Ag–Bi–I thin films produced on a TiO₂/FTO/glass substrate.⁵⁸ The appearance of the AgI phase

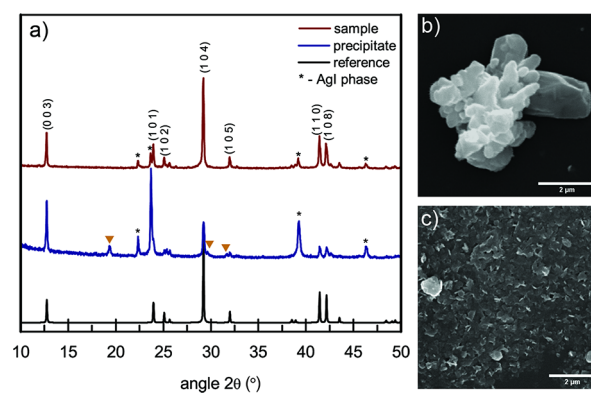


Figure 1. (a) XRD patterns of Ag–Bi–I powder (red line) and the precipitate sample obtained by drying Ag–Bi–I acetonitrile dispersion under ambient conditions (blue line). The black line represents the Ag₃BiI₆ reference pattern.⁵⁶ The asterisks and triangles mark the 2θ angles corresponding to the diffraction maxima of the AgI phase²⁰ and the BiOI phase,⁵⁸ respectively. SEM images of (b) Ag–Bi–I powder and (c) precipitate samples.

in the sample is expected since in the Ag-rich Ag–Bi–I solids, the excess of Ag ions are delocalized and occupy the sites between the (Ag/Bi)I₆ octahedral layers.¹⁹ The XRD measurements were performed on a precipitate of the Ag–Bi–I sample in order to check its structure after dispersion in acetonitrile. This sample is prepared by drying the colloid in the dark under ambient conditions. The XRD pattern of the precipitate (Figure 1a, blue line) shows that in addition to the increase in the AgI content, the sample retained its Ag–Bi–I phase. Changes in morphology were also investigated by SEM, and the images of two samples are shown in Figure 1b,c. These analyses showed that exfoliation of Ag–Bi–I sheets upon dispersion in acetonitrile takes place, which is consistent with an increase in the intensity of (0 0 3) diffraction maximum relative to the (1 0 4) peak in the diffractogram of the precipitate. In addition, the presence of the bismuth oxyiodide (BiOI) phase in the diffraction pattern can be seen, resulting from drying the sample in air. This result indicates that oxidation occurs at the outmost layers of the exfoliated particles.

Further analyses of the size and morphology of the dispersed-phase Ag–Bi–I particles were carried out by transmission electron microscopy on the colloidal samples dried in a vacuum. Typical TEM images of the sample are presented in Supporting Information Figure S2. For comparison, the results for BiI₃ particles, prepared using the same procedure, are also given. The micrographs show that the Ag–Bi–I particles have a plate-like morphology with average lateral dimensions of \sim 160 nm. A similar morphology was also observed for BiI₃ nanoparticles; however, their lateral dimensions were in the 40–60 nm range. The observed morphology is characteristic of binary metal iodides (such as BiI₃^{41,59}) and occurs because of a relatively large difference in distance between cations in edge-sharing octahedra and the distance between cations in adjacent layers. In rudorffite Ag_{2–3x}Bi_xI₂ ($x = 0.33–0.60$) ternary halides, Ag and Bi ions occupy similar edge-sharing octahedral sites (Ag/Bi)I₆,^{15,19} which results in the formation of the Ag–Bi–I nanoplatelets. The HRTEM/EDS mapping of Ag–Bi–I nanoplatelets (Supporting information Figure S2c) showed that the elements were uniformly distributed in the particles. The distribution of the thicknesses of the nanoplatelets was determined from their

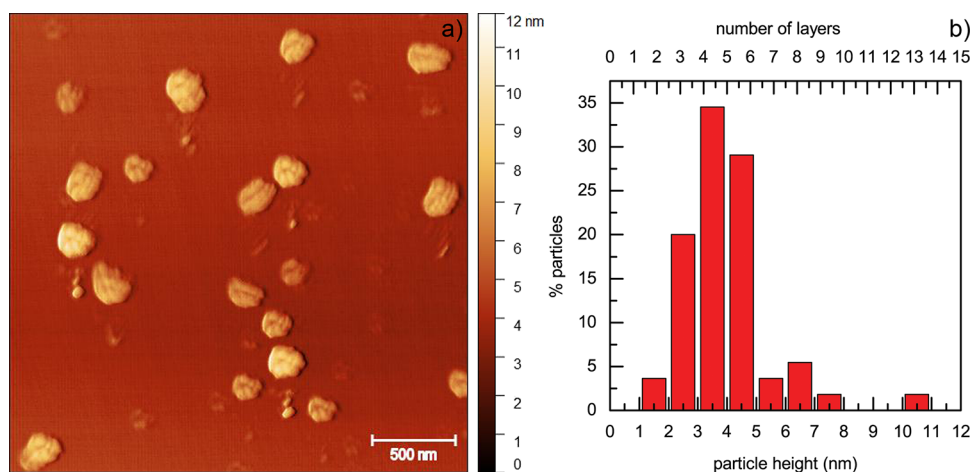


Figure 2. (a) AFM image of Ag–Bi–I nanoplatelets and (b) corresponding distribution of particles' heights. The number of Ag–Bi–I monolayers in the nanoplatelets was estimated assuming a monolayer thickness of 0.66 nm.

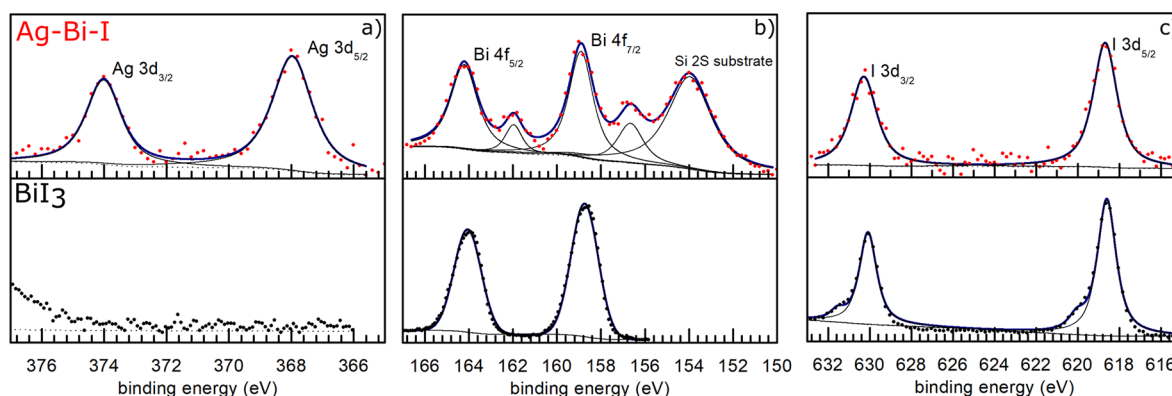


Figure 3. High-resolution XPS spectra of (a) Ag 3d, (b) Bi 4f, and (c) I 3d core levels of Ag–Bi–I (top) and BiI₃ (bottom) colloidal nanoplatelets.

height profiles obtained by AFM. The AFM image of the Ag–Bi–I sample and the particle height distribution are presented in Figure 2a,b, respectively, while the details of the height profile analyses are given in the Supporting Information (Figure S3). The average thickness of the nanoplatelets was found to be 3.9 ± 0.2 nm. Taking into account that the thickness of the monolayer is ~ 0.66 nm, the nanoplatelets, on average, have six layers.

The chemical environment of the ions in the Ag–Bi–I nanoplatelets was investigated by surface X-ray photoelectron spectroscopy. High-resolution XPS spectra of the Ag 3d, Bi 4f, and I 3d core levels of the Ag–Bi–I nanoplatelets are presented in Figure 3. The survey scan of the sample is given in Supporting Information Figure S4. For comparison, the results for the BiI₃ sample are also shown. For the Ag–Bi–I sample, Ag 3d_{3/2} and Ag 3d_{5/2} levels are observed at 374.0 and 368.0 eV, respectively (Figure 3a). These values match the binding energies obtained for Ag 3d levels in AgI.⁶⁰ For Bi, 4f levels (Figure 3b) are assigned to peaks at 164.2 and 158.9 eV, corresponding to Bi 4f_{5/2} and Bi 4f_{7/2} levels. The spectrum shows additional peaks at lower binding energies that are not present for the BiI₃ sample. These features were previously reported for the Ag–Bi–I films prepared by thermal evaporation⁶¹ as well as for the oriented BiI₃ single crystals in contact with Pd and Pt.⁶² The peaks were assigned to bismuth ions that are not in a complete 6I⁺ coordination and therefore approach binding energies characteristic for metallic

bismuth. The binding energies of I 3d_{3/2} and I 3d_{5/2} levels are observed at 630.3 and 618.7 eV (Figure 3c). It should be noticed that the I 3d levels in the Ag–Bi–I sample are slightly broader than in the BiI₃ sample, suggesting possible effects of changes in the chemical environment. The XPS results suggest that a redox solid-state reaction between Ag and BiI₃ is taking place in the system, resulting in the formation of Ag–Bi–I and AgI phases, as well as metallic Bi (which can proceed to the formation of BiOI in the presence of oxygen), noticed in the XRD pattern (Figure 1). A similar redox reaction was observed at the interfaces between Ag and Bi₂Se₃ single crystals.⁶³

Electronic Properties of the Ag–Bi–I Nanoplatelets.

To study the electronic properties of Ag–Bi–I nanoplatelets in the valence region, we used a similar approach as in our previous study of MAPbBr₃ nanoparticles.¹ Two complementary X-ray photoemission spectroscopy techniques were employed. For XPS measurements, the colloids were deposited onto a Si substrate. The XAPS measurements were carried out on isolated Ag–Bi–I particles, where synchrotron radiation was used as the X-ray source.

The photoemission spectrum of Ag–Bi–I nanoplatelets obtained by the XAPS technique is presented in Figure 4, while the corresponding spectrum of the BiI₃ sample is given in the Supporting Information (Figure S5a). Contrary to XPS measurements, where the band energies are referenced with respect to the Fermi level (E_F), all energies in the XAPS technique are measured with respect to the vacuum level (E_0).¹

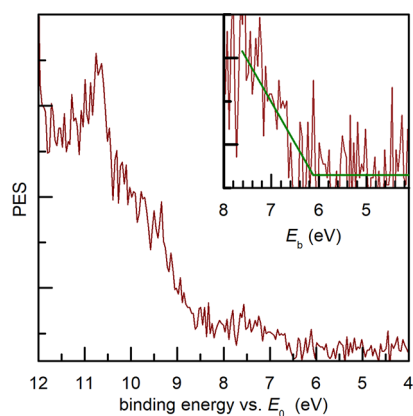


Figure 4. Valence region photoemission spectrum of Ag–Bi–I nanoplatelets measured by XAPS using 100 eV photon energy. The inset shows the zoom-in region around the ionization energy value.

The ionization energy of Ag–Bi–I nanoplatelets determined by XAPS is 6.1 ± 0.2 eV relative to E_0 . This is in good agreement with the ionization energies reported for 3D Ag_3BiI_6 aerosol particles²⁷ and Ag_3BiI_6 thin films⁵⁸ as well as those reported for rhombohedral $\text{Ag}_{0.65}\text{Bi}_{0.45}\text{I}_2$ materials.¹⁹ This indicates a negligible influence of the size and morphology of Ag–Bi–I particles on the position of the valence band maxima. The ionization energy is also in good agreement with our calculated value of -5.95 eV for the valence band maximum. The ionization energy obtained by surface XPS was 1.4 ± 0.2 eV relative to E_F (Supporting Information Figure S5b). By comparing the values of the ionization energies obtained by these two techniques, the estimated value of the work function (ϕ) of Ag–Bi–I nanoplatelets was found to be 4.7 eV. It should be noted, however, that in the XAPS of isolated nanoparticles, the near-surface vacuum level cannot be perfectly defined, which results in additional uncertainty in the determination of the ionization energy.^{64,65}

The optical properties of the Ag–Bi–I powder and the colloidal dispersion in acetonitrile are presented in Figure 5. The diffuse reflectance spectrum of the Ag–Bi–I powder samples (dashed black line) displays an onset of absorption at 732 nm (~ 1.7 eV), which is a typical value for the band gap of Ag–Bi–I thin films and powder samples.^{15,21,23} After exfoliation, the UV–vis absorption spectrum of the Ag–Bi–I

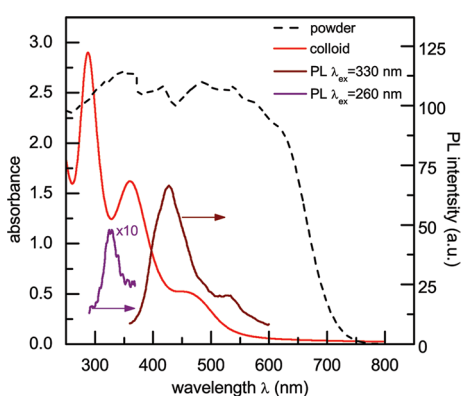


Figure 5. UV–vis absorption (red line) and photoluminescence (PL) (purple and brown lines) spectra of Ag–Bi–I nanoplatelets dispersed in acetonitrile and the diffuse reflectance spectrum of Ag–Bi–I powders (dashed black line).

colloid (solid red line) shows three bands at 288 nm (4.30 eV), 360 nm (3.44 eV), and 457 nm (2.71 eV). The bands in the spectra of the Ag–Bi–I colloid originate mainly from I 5p to Bi 6p and I 5p to I 5p transitions in $(\text{BiI}_6)^{3-}$ octahedra. It should be noted that the absorption spectra obtained for BiI_3 powder and its dispersion in acetonitrile are similar to those obtained for corresponding Ag–Bi–I samples (Supporting Information Figure S7). The absorption spectrum of the BiI_3 powder (Figure S7) exhibited a slightly lower band gap value, which is in accordance with the results presented in the literature.⁶¹ On the other hand, the absorption spectrum of the BiI_3 dispersion has similar features as the spectrum of the Ag–Bi–I colloid, although the absorption peaks appear at slightly different energies. It seems that the changes induced by the additional element in the structure affect I 5p to Bi 6p and I 5p to I 5p transitions to a certain extent. A recent study by Kanatzidis et al.²⁸ may support this conclusion. They showed that the optical properties of 2D Ag–Bi–I layered materials significantly depend on both the distance between the layers and the arrangement and orientation of $(\text{AgI}_6)^{5-}$ and $(\text{BiI}_6)^{3-}$ octahedra.

Recently, Premkumar et al. synthesized Ag–Bi–I quantum dots and noticed that they exhibited blueshifted absorption with respect to the bulk material.⁶⁶ The observed shift is attributed to the size confinement effect. However, because the effective masses of the charge carriers in Ag–Bi–I material are relatively large,⁵⁸ it can be expected that the quantum confinement effects in the Ag–Bi–I nanoplatelets are relatively weak. Indeed, our calculations (see Figure 7 below) showed that the nanoplatelet band gap changes by only about 50 meV in the range of thicknesses from 2 to 5 nm. This suggests that the three peaks at 2.71, 3.44, and 4.30 eV are the internal transitions already present in the bulk sample as well, which become more pronounced after exfoliation. To check this, we made a rough calculation of the optical absorption for the bulk Ag–Bi–I (see Supporting Information Figure S6). The theoretical absorption curve in Figure S6 exhibits a similar trend as the experimental absorption spectrum of Ag–Bi–I colloid in the UV–vis range.

The photoluminescence spectra of the Ag–Bi–I nanoplatelets dispersed in acetonitrile, recorded with 260 nm (purple solid line) and 330 nm (brown solid line) excitations, are also presented in Figure 5. The emission bands at around 326, 430, and 530 nm are Stokes-shifted with respect to the band observed in the absorption spectrum. The excitation of the colloids by the light of different wavelengths did not affect the position of the emission bands (Supporting Information Figure S8). Notably, the emission at the photon energy of the band gap was not detected in either powder or colloid samples.

DFT was used to calculate the electronic structure of Ag–Bi–I nanoplatelets. The calculations of the electronic structure of the platelets with larger lateral dimensions were performed by the $\mathbf{k} \cdot \mathbf{p}$ method, and the Hamiltonian parameterization was carried out using the results obtained by the DFT. As a model for the atomic structure of the Ag–Bi–I material, we used the rhombohedral AgBiI_4 configuration. The details about its atomic structure, corresponding lattice parameters, and atomic positions are given in the Supporting Information.

The electronic band structure of bulk AgBiI_4 obtained from DFT/PBE calculations is presented in Figure 6a. A direct band gap can be observed at the Y_2 point in the Brillouin zone with a band gap energy of 0.33 eV was found. As expected, the DFT/PBE calculation yields a significantly lower value of the band

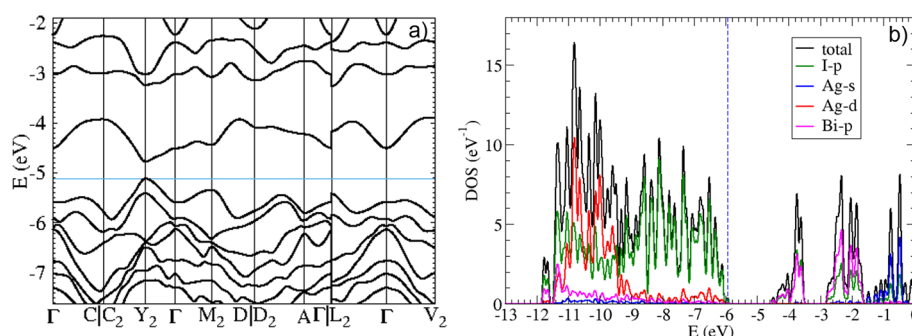


Figure 6. (a) Electronic band structure of AgBiI_4 obtained from DFT/PBE calculations. The blue horizontal line represents the valence band maximum energy. The choice of the path in the Brillouin zone was made using the SeeK-path tool.⁶⁷ (b) Density of electronic states (total density of states and orbital projected density of states) of AgBiI_4 obtained from hybrid PBE0 functional calculations. The vertical dashed line denotes the energy of the valence band maximum. The reported energy values in figures (a) and (b) are given with respect to the vacuum level.

gap than the energy value established in the experiment. For this reason, an additional approach was considered, and the calculation was performed using the hybrid PBE0 functional. In this calculation, the band gap energy of 1.3 eV was obtained, which is much closer to the experimental result of 1.7 eV. The calculated densities of electronic states are presented in Figure 6b. The results suggest that the highest states in the valence band (in the energy interval of ~ 3 eV below the valence band maximum) originate from p-orbitals of the I atom, while the lowest states in the conduction band (in the energy interval of ~ 2.5 eV above the conduction band minimum) originate from p-orbitals of the Bi and I atoms. This result is in agreement with the previous reports^{23,28} and supports the claim that the optical transitions in Ag–Bi–I are dominated by I 5p to Bi 6p and by I 5p to I 5p transitions in the $(\text{BiI}_6)^{3-}$.

Since the lateral dimensions of the Ag–Bi–I nanoplatelets are much larger than vertical dimensions (Figure 2), they were modeled as quantum wells infinite in the xy plane with width L in the z -direction. The procedure for constructing their atomic structure is presented in the Supporting Information. Three different methods were employed to calculate the electronic structure of AgBiI_4 quantum wells: (i) DFT/PBE; (ii) $\mathbf{k} \cdot \mathbf{p}$ method with parameterization based on DFT/PBE calculations of bulk AgBiI_4 ; (iii) $\mathbf{k} \cdot \mathbf{p}$ calculations with parameterization based on hybrid PBE0 functional calculations of bulk AgBiI_4 .

The results obtained by using method (i) are presented in the Supporting Information. This method cannot give accurate values of the band gap, but it is still useful for gaining insight into the overall role of quantum confinement effects. The results indicate that these effects are quite weak. In the range of well widths of 2 to 5 nm (corresponding to the range of the heights of the nanoplatelets that were observed), the band gap changes for about 50 meV only (see Figure S12 in the Supporting Information). The comparison of the band structures of quantum wells with different widths (Figures S13 and S14 in the Supporting Information) also suggests that the electronic structure is only weakly dependent on the well width. Therefore, within a reasonably good approximation, it follows that the electronic structure of the nanoplatelet is rather similar to the electronic structure of the bulk material.

The calculations using method (ii) were used to confirm that the $\mathbf{k} \cdot \mathbf{p}$ method is reliable for the calculation of electronic states in quantum wells. Details of this calculation are reported in the Supporting Information. The results suggest that $\mathbf{k} \cdot \mathbf{p}$

and DFT/PBE yield essentially the same results for well widths above 2 nm, which implies that $\mathbf{k} \cdot \mathbf{p}$ can be safely used then.

Finally, method (iii) was employed to calculate the band gap, conduction band minimum (CBM), and valence band maximum (VBM) of the quantum wells of various sizes. The results (Figure 7) indicate a rather weak dependence of

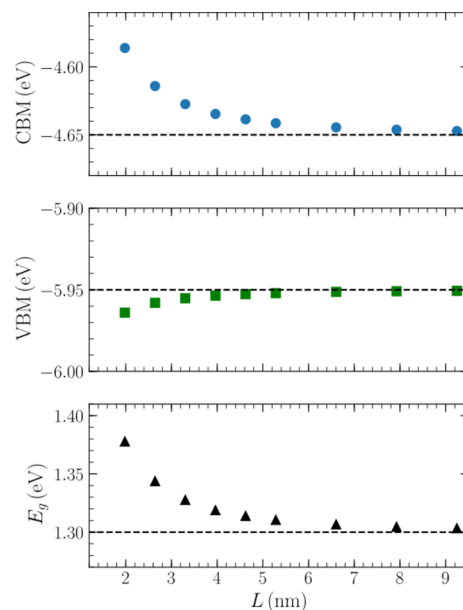


Figure 7. The dependence of CBM, VBM, and energy gap (E_g) on quantum well width. The results were obtained from the $\mathbf{k} \cdot \mathbf{p}$ Hamiltonian parameterized using the data from hybrid PBE0 functional calculations of bulk Ag–Bi–I. Horizontal dashed lines denote the bulk values.

electronic states energies on the well width, consistent with previous conclusions obtained by using less accurate methods. It was also estimated that the dielectric contrast between the nanoplatelet and the solvent does not affect the energy levels of the nanoplatelet to a significant extent (see the Supporting Information for details).

CONCLUSIONS

In summary, we report a simple procedure for the chemical exfoliation of sliver/bismuth iodide powders into Ag–Bi–I nanoplatelets dispersible in acetonitrile together with results of characterization and electronic structure determination.

The XRD results showed that the material prepared is composed of a rhombohedral Ag-rich ruderfite phase with minor traces of the γ -AgI phase. The results of the morphological characterization revealed that the material is in the form of layered two-dimensional nanoplatelets with lateral dimensions of ~ 160 nm and thicknesses in the 1–8 nm range, indicating that the prepared nanoplatelets consist of 1–10 Ag–Bi–I monolayers. XPS analyses of the Ag 3d, Bi 4f, and I 3d core levels suggested that the Ag–Bi–I ruderfite phase is being formed by a redox reaction between Ag and BiI₃, which also results in the formation of γ -AgI and metallic Bi phases. The valence band electronic structure of isolated Ag–Bi–I nanoplatelets was investigated by synchrotron radiation X-ray aerosol photoelectron spectroscopy. An ionization energy of 6.1 ± 0.2 eV was obtained with respect to the vacuum level. The value of the ionization energy was found to be 1.4 ± 0.2 eV with respect to the Fermi level by standard XPS. We therefore estimated the work function of Ag–Bi–I nanoplatelets to be 4.7 eV. The band gap value of Ag–Bi–I powder was estimated to be ~ 1.7 eV based on the diffuse reflectance spectrum. The UV–vis absorption spectroscopy of the Ag–Bi–I colloids showed that the optical properties of the nanoplatelets originate mainly from I 5p to Bi 6p and I 5p to I 5p transitions, which is further confirmed by DFT calculations. To interpret the electronic properties of the Ag–Bi–I nanoplatelets with larger lateral dimensions, we performed electronic structure calculations using the density functional theory and $\mathbf{k} \cdot \mathbf{p}$ methods. The DFT results showed weak dependence of the ionization energy and the band gap values of Ag–Bi–I nanoplatelets on their thickness.

This work demonstrates a simple and innovative route for the preparation of colloidal 2D layered Ag–Bi–I nanomaterials. In addition, the study offers a deeper insight into the understanding of the electronic structure of the Ag–Bi–I nanoplatelets, which were further correlated with the particle size.

■ ASSOCIATED CONTENT

SI Supporting Information

The Supporting Information is available free of charge at <https://pubs.acs.org/doi/10.1021/acs.jpcc.2c03208>.

Images of Ag–Bi–I powder and Ag–Bi–I dispersed in acetonitrile; results of TEM and EDS analyses; AFM images with AFM profile analysis of Ag–Bi–I nanoplatelets; XPS survey scan of Ag–Bi–I nanoplatelets; valence region XPS spectra of Ag–Bi–I and BiI₃ nanoparticles; comparison of calculations with experimental absorption spectra; absorption spectra of Ag–Bi–I and BiI₃ powders and their dispersion in acetonitrile; PL spectra of Ag–Bi–I dispersed in acetonitrile; details of DFT calculations (PDF)

■ AUTHOR INFORMATION

Corresponding Authors

Aleksandar R. Milosavljević – *Synchrotron SOLEIL, l'Orme des Merisiers, 91192 Gif sur Yvette Cedex, France*;
orcid.org/0000-0003-3541-8872; Email: milosavljevic@synchrotron-soleil.fr

Dušan K. Božanić – *Department of Radiation Chemistry and Physics, "Vinča" Institute of Nuclear Sciences - National Institute of the Republic of Serbia and Center of Excellence for Photoconversion, "Vinča" Institute of Nuclear Sciences -*

National Institute of the Republic of Serbia, University of Belgrade, 11001 Belgrade, Serbia; orcid.org/0000-0001-8246-9635; Email: bozanic@vin.bg.ac.rs

Authors

Danijela Danilović – *Department of Radiation Chemistry and Physics, "Vinča" Institute of Nuclear Sciences - National Institute of the Republic of Serbia and Center of Excellence for Photoconversion, "Vinča" Institute of Nuclear Sciences - National Institute of the Republic of Serbia, University of Belgrade, 11001 Belgrade, Serbia*

Pitambar Sapkota – *Radiation Laboratory, University of Notre Dame, Notre Dame, Indiana 46556, United States; Department of Physics, University of Notre Dame, Notre Dame, Indiana 46556, United States*

Radovan Dojčilović – *Department of Radiation Chemistry and Physics, "Vinča" Institute of Nuclear Sciences - National Institute of the Republic of Serbia and Center of Excellence for Photoconversion, "Vinča" Institute of Nuclear Sciences - National Institute of the Republic of Serbia, University of Belgrade, 11001 Belgrade, Serbia; Department of Experimental and Health Sciences, Pompeu Fabra University, 08003 Barcelona, Spain*

Dragana Tošić – *Department of Radiation Chemistry and Physics, "Vinča" Institute of Nuclear Sciences - National Institute of the Republic of Serbia, University of Belgrade, 11001 Belgrade, Serbia*

Enad Vukmirović – *Institute of Physics Belgrade, University of Belgrade, 11080 Belgrade, Serbia*; orcid.org/0000-0002-4101-1713

Milan Jocić – *Institute of Physics Belgrade, University of Belgrade, 11080 Belgrade, Serbia*

Vladimir Djoković – *Department of Radiation Chemistry and Physics, "Vinča" Institute of Nuclear Sciences - National Institute of the Republic of Serbia and Center of Excellence for Photoconversion, "Vinča" Institute of Nuclear Sciences - National Institute of the Republic of Serbia, University of Belgrade, 11001 Belgrade, Serbia*

Sylwia Ptasinska – *Radiation Laboratory, University of Notre Dame, Notre Dame, Indiana 46556, United States; Department of Physics, University of Notre Dame, Notre Dame, Indiana 46556, United States*; orcid.org/0000-0002-7550-8189

Complete contact information is available at:
<https://pubs.acs.org/doi/10.1021/acs.jpcc.2c03208>

Notes

The authors declare no competing financial interest.

■ ACKNOWLEDGMENTS

The authors acknowledge funding from the Ministry of Education, Science, and Technological Development of the Republic of Serbia. The authors are grateful for the support of the entire staff of the Synchrotron SOLEIL for smooth operation during beamtime no. 20190421. Numerical simulations were performed on the PARADOX supercomputing facility at the Scientific Computing Laboratory, National Center of Excellence for the Study of Complex Systems, Institute of Physics Belgrade. P.S. and S.P. acknowledge the US Department of Energy Office of Science, Office of Basic Energy Sciences under award number DE-FC02-04ER15533 (NDRL no. 5356).

REFERENCES

- (1) Milosavljević, A. R.; Božanić, D. K.; Sadhu, S.; Vukmirović, N.; Dojčilović, R.; Sapkota, P.; Huang, W.; Bozek, J.; Nicolas, C.; Nahon, L.; et al. Electronic Properties of Free-Standing Surfactant-Capped Lead Halide Perovskite Nanocrystals Isolated in Vacuo. *J. Phys. Chem. Lett.* **2018**, *9*, 3604–3611.
- (2) Mei, A.; Li, X.; Liu, L.; Ku, Z.; Liu, T.; Rong, Y.; Xu, M.; Hu, M.; Chen, J.; Yang, Y.; et al. A Hole-Conductor-Free, Fully Printable Mesoscopic Perovskite Solar Cell with High Stability. *Science* **2014**, *345*, 295–298.
- (3) Leung, S.-F.; Ho, K.-T.; Kung, P.-K.; Hsiao, V. K. S.; Alshareef, H. N.; Wang, Z. L.; He, J.-H. A Self-Powered and Flexible Organometallic Halide Perovskite Photodetector with Very High Detectivity. *Adv. Mater.* **2018**, *30*, 1704611.
- (4) Chen, Q.; de Marco, N.; Yang, Y. M.; Song, T.-B.; Chen, C.-C.; Zhao, H.; Hong, Z.; Zhou, H.; Yang, Y. Under the Spotlight: The Organic-Inorganic Hybrid Halide Perovskite for Optoelectronic Applications. *Nano Today* **2015**, *10*, 355–396.
- (5) Yuan, M.; Quan, L. N.; Comin, R.; Walters, G.; Sabatini, R.; Voznyy, O.; Hoogland, S.; Zhao, Y.; Beauregard, E. M.; Kanjanaboos, P.; et al. Perovskite Energy Funnels for Efficient Light-Emitting Diodes. *Nat. Nanotechnol.* **2016**, *11*, 872–877.
- (6) Yang, W. S.; Park, B.-W.; Jung, E. H.; Jeon, N. J.; Kim, Y. C.; Lee, D. U.; Shin, S. S.; Seo, J.; Kim, E. K.; Noh, J. H.; Seok, S. I. Iodide Management in Formamidinium-Lead-Halide-Based Perovskite Layers for Efficient Solar Cells. *Science* **2017**, *356*, 1376–1379.
- (7) NREL. Best Research-Cell Efficiency Chart. <https://www.nrel.gov/pv/cell-efficiency.html> (accessed February 2, 2022).
- (8) Brandt, R. E.; Stevanović, V.; Ginley, D. S.; Buonassisi, T. Identifying Defect-Tolerant Semiconductors with High Minority-Carrier Lifetimes: Beyond Hybrid Lead Halide Perovskites. *MRS Commun.* **2015**, *5*, 265–275.
- (9) Aristidou, N.; Sanchez-Molina, I.; Chotchuangchutchaval, T.; Brown, M.; Martinez, L.; Rath, T.; Haque, S. A. The Role of Oxygen in the Degradation of Methylammonium Lead Trihalide Perovskite Photoactive Layers. *Am. Ethnol.* **2015**, *127*, 8326–8330.
- (10) Habisreutinger, S. N.; Leijtens, T.; Eperon, G. E.; Stranks, S. D.; Nicholas, R. J.; Snaith, H. J. Carbon Nanotube/Polymers Composites as a Highly Stable Hole Collection Layer in Perovskite Solar Cells. *Nano Lett.* **2014**, *14*, 5561–5568.
- (11) Bag, M.; Renna, L. A.; Adhikari, R. Y.; Karak, S.; Liu, F.; Lahti, P. M.; Russell, T. P.; Tuominen, M. T.; Venkataraman, D. Kinetics of Ion Transport in Perovskite Active Layers and Its Implications for Active Layer Stability. *J. Am. Chem. Soc.* **2015**, *137*, 13130–13137.
- (12) Chaudhary, B.; Kulkarni, A.; Jena, A. K.; Ikegami, M.; Udagawa, Y.; Kunugita, H.; Ema, K.; Miyasaka, T. Poly(4-Vinylpyridine)-Based Interfacial Passivation to Enhance Voltage and Moisture Stability of Lead Halide Perovskite Solar Cells. *ChemSusChem* **2017**, *10*, 2473–2479.
- (13) Milosavljević, A. R.; Huang, W.; Sadhu, S.; Ptasinska, S. Low-Energy Electron-Induced Transformations in Organolead Halide Perovskite. *Angew. Chem., Int. Ed.* **2016**, *55*, 10083–10087.
- (14) Babayigit, A.; Ethirajan, A.; Muller, M.; Conings, B. Toxicity of Organometal Halide Perovskite Solar Cells. *Nat. Mater.* **2016**, *15*, 247–251.
- (15) Turkevych, I.; Kazaoui, S.; Ito, E.; Urano, T.; Yamada, K.; Tomiyasu, H.; Yamagishi, H.; Kondo, M.; Aramaki, S. Photovoltaic Rudorffites: Lead-Free Silver Bismuth Halides Alternative to Hybrid Lead Halide Perovskites. *ChemSusChem* **2017**, *10*, 3754–3759.
- (16) Oh, J. T.; Kim, D. H.; Kim, Y. Solution-Processed “silver-Bismuth-Iodine” Ternary Thin Films for Lead-Free Photovoltaic Absorbers. *J. Visualized Exp.* **2018**, *2018*, No. e58286.
- (17) Hosseini, S. S.; Adelifard, M.; Atefi, M. An Investigation on Physical Properties of Ag₂BiI₅ Absorber Layers Synthesized by Microwave Assisted Spin Coating Technique. *J. Mater. Sci.: Mater. Electron.* **2019**, *30*, S021–S029.
- (18) Jung, K. W.; Sohn, M. R.; Lee, H. M.; Yang, I. S.; Sung, S. D.; Kim, J.; Wei-Guang Diao, E.; Lee, W. I. Silver Bismuth Iodides in Various Compositions as Potential Pb-Free Light Absorbers for Hybrid Solar Cells. *Sustainable Energy Fuels* **2018**, *2*, 294–302.
- (19) Koedtruid, A.; Goto, M.; Amano Patino, M.; Tan, Z.; Guo, H.; Nakamura, T.; Handa, T.; Chen, W. T.; Chuang, Y. C.; Sheu, H. S.; et al. Structure-Property Relations in Ag–Bi–I Compounds: Potential Pb-Free Absorbers in Solar Cells. *J. Mater. Chem. A* **2019**, *7*, 5583–5588.
- (20) Mashadiev, L. F.; Aliev, Z. S.; Shevelkov, A. V.; Babanly, M. B. Experimental Investigation of the Ag–Bi–I Ternary System and Thermodynamic Properties of the Ternary Phases. *J. Alloys Compd.* **2013**, *551*, 512–520.
- (21) Ghosh, B.; Wu, B.; Guo, X.; Harikesh, P. C.; John, R. A.; Baikie, T.; Wee, A. T.; Guet, C.; Sum, T. C.; et al. Superior Performance of Silver Bismuth Iodide Photovoltaics Fabricated via Dynamic Hot-Casting Method under Ambient Conditions. *Adv. Energy Mater.* **2018**, *8*, 1802051.
- (22) Lu, C.; Zhang, J.; Sun, H.; Hou, D.; Gan, X.; Shang, M. H.; Li, Y.; Hu, Z.; Zhu, Y.; Han, L. Inorganic and Lead-Free AgBiI₄ Rudorffite for Stable Solar Cell Applications. *ACS Appl. Energy Mater.* **2018**, *1*, 4485–4492.
- (23) Sansom, H. C.; Whitehead, G. F. S.; Dyer, M. S.; Zanella, M.; Manning, T. D.; Pitcher, M. J.; Whittles, T. J.; Dhanak, V. R.; Alaria, J.; Claridge, J. B.; et al. AgBiI₄ as a Lead-Free Solar Absorber with Potential Application in Photovoltaics. *Chem. Mater.* **2017**, *29*, 1538–1549.
- (24) Zhang, Q.; Wu, C.; Qi, X.; Lv, F.; Zhang, Z.; Liu, Y.; Wang, S.; Qu, B.; Chen, Z.; Xiao, L. Photovoltage Approaching 0.9 V for Planar Heterojunction Silver Bismuth Iodide Solar Cells with Li-TFSI Additive. *ACS Appl. Energy Mater.* **2019**, *2*, 3651–3656.
- (25) Zhu, H.; Pan, M.; Johansson, M. B.; Johansson, E. M. J. High Photon-to-Current Conversion in Solar Cells Based on Light-Absorbing Silver Bismuth Iodide. *ChemSusChem* **2017**, *10*, 2592–2596.
- (26) Iyoda, F.; Nishikubo, R.; Wakamiya, A.; Saeki, A. Ag-(Bi, Sb, In, Ga)-I Solar Cells: Impacts of Elemental Composition and Additives on the Charge Carrier Dynamics and Crystal Structures. *ACS Appl. Energy Mater.* **2020**, *3*, 8224–8232.
- (27) Danilović, D.; Božanić, D. K.; Dojčilović, R.; Vukmirović, N.; Sapkota, P.; Vukašinović, I.; Djoković, V.; Bozek, J.; Nicolas, C.; Ptasinska, S.; et al. Aerosol Synthesis and Gas-Phase Photoelectron Spectroscopy of Ag–Bi–I Nanosystems. *J. Phys. Chem. C* **2020**, *124*, 23930–23937.
- (28) Li, X.; Traoré, B.; Kepenekian, M.; Li, L.; Stoumpos, C. C.; Guo, P.; Even, J.; Katan, C.; Kanatzidis, M. G. Bismuth/Silver-Based Two-Dimensional Iodide Double and One-Dimensional Bi Perovskites: Interplay between Structural and Electronic Dimensions. *Chem. Mater.* **2021**, *33*, 6206–6216.
- (29) Tyagi, P.; Arveson, S. M.; Tisdale, W. A. Colloidal Organohalide Perovskite Nanoplatelets Exhibiting Quantum Confinement. *J. Phys. Chem. Lett.* **2015**, *6*, 1911–1916.
- (30) Huang, C.; Gao, Y.; Wang, S.; Zhang, C.; Yi, N.; Xiao, S.; Song, Q. Giant Blueshifts of Excitonic Resonances in Two-Dimensional Lead Halide Perovskite. *Nano Energy* **2017**, *41*, 320–326.
- (31) Ding, Y.-F.; Zhao, Q.-Q.; Yu, Z.-L.; Zhao, Y.-Q.; Liu, B.; He, P.-B.; Zhou, H.; Li, K.; Yin, S.-F.; Cai, M.-Q. Strong Thickness-Dependent Quantum Confinement in All-Inorganic Perovskite Cs₂PbI₄ with a Ruddlesden–Popper Structure. *J. Mater. Chem. C* **2019**, *7*, 7433–7441.
- (32) Connor, B. A.; Leppert, L.; Smith, M. D.; Neaton, J. B.; Karunadasa, H. I. Layered Halide Double Perovskites: Dimensional Reduction of Cs₂AgBiBr₆. *J. Am. Chem. Soc.* **2018**, *140*, 5235–5240.
- (33) Gelmetti, I.; Cabau, L.; Montcada, N. F.; Palomares, E. Selective Organic Contacts for Methyl Ammonium Lead Iodide (MAPI) Perovskite Solar Cells: Influence of Layer Thickness on Carriers Extraction and Carriers Lifetime. *ACS Appl. Mater. Interfaces* **2017**, *9*, 21599–21605.
- (34) Bekenstein, Y.; Dahl, J. C.; Huang, J.; Osowiecki, W. T.; Swabeck, J. K.; Chan, E. M.; Yang, P.; Alivisatos, A. P. The Making and Breaking of Lead-Free Double Perovskite Nanocrystals of Cesium

Silver–Bismuth Halide Compositions. *Nano Lett.* **2018**, *18*, 3502–3508.

(35) Tan, Z.; Wu, Y.; Hong, H.; Yin, J.; Zhang, J.; Lin, L.; Wang, M.; Sun, X.; Sun, L.; Huang, Y.; et al. Two-Dimensional $(\text{C}_4\text{H}_9\text{NH}_3)_2\text{PbBr}_4$ Perovskite Crystals for High-Performance Photodetector. *J. Am. Chem. Soc.* **2016**, *138*, 16612–16615.

(36) Creutz, S. E.; Crites, E. N.; de Siena, M. C.; Gamelin, D. R. Colloidal Nanocrystals of Lead-Free Double-Perovskite (Elpasolite) Semiconductors: Synthesis and Anion Exchange To Access New Materials. *Nano Lett.* **2018**, *18*, 1118–1123.

(37) Pal, J.; Bhunia, A.; Chakraborty, S.; Manna, S.; Das, S.; Dewan, A.; Datta, S.; Nag, A. Synthesis and Optical Properties of Colloidal $\text{M}_3\text{Bi}_2\text{I}_9$ ($\text{M} = \text{Cs}, \text{Rb}$) Perovskite Nanocrystals. *J. Phys. Chem. C* **2018**, *122*, 10643–10649.

(38) Brus, L. E. Electron-Electron and Electron-Hole Interactions in Small Semiconductor Crystallites: The Size Dependence of the Lowest Excited Electronic State. *Chem. Phys.* **1984**, *80*, 4403–4409.

(39) Sandroff, C. J.; Kelty, S. P.; Hwang, D. M. Clusters in Solution: Growth and Optical Properties of Layered Semiconductors with Hexagonal and Honeycombed Structures. *Chem. Phys.* **1986**, *85*, 5337–5340.

(40) Micic, O. I.; Nenadovic, M. T.; Peterson, M. W.; Nozik, A. J. Size Quantization in Layered Semiconductor Colloids with Tetrahedral Bonding: Mercury Diiodide. *J. Phys. Chem.* **1987**, *91*, 1295–1297.

(41) Micic, O. I.; Li, Z.; Mills, G.; Sullivan, J. C.; Meisel, D. Formation of Small Particles of Lead Iodide, Mercuric Iodide, and Bismuth Iodide Layered Semiconductors. *J. Phys. Chem.* **1987**, *91*, 6221–6229.

(42) Liu, Z.; Yang, H.; Wang, J.; Yuan, Y.; Hills-Kimball, K.; Cai, T.; Wang, P.; Tang, A.; Chen, O. Synthesis of Lead-Free $\text{Cs}_2\text{AgBiX}_6$ ($\text{X} = \text{Cl}, \text{Br}, \text{I}$) Double Perovskite Nanoplatelets and Their Application in CO_2 Photocatalytic Reduction. *Nano Lett.* **2021**, *21*, 1620–1627.

(43) Božanić, D. K.; Garcia, G. A.; Sublemontier, O.; Pajović, J.; Djoković, V.; Nahon, L. Velocity Map Imaging VUV Angle-Resolved Photoemission on Isolated Nanosystems: Case of Gold Nanoparticles. *J. Phys. Chem. C* **2020**, *124*, 24500–24512.

(44) Perdew, J. P.; Burke, K.; Ernzerhof, M. Generalized Gradient Approximation Made Simple. *Phys. Rev. Lett.* **1996**, *77*, 3865–3868.

(45) van Setten, M. J.; Giantomassi, M.; Bousquet, E.; Verstraete, M. J.; Hamann, D. R.; Gonze, X.; Rignanese, G.-M. The PseudoDojo: Training and Grading a 85 Element Optimized Norm-Conserving Pseudopotential Table. *Comput. Phys. Commun.* **2018**, *226*, 39–54.

(46) Hamann, D. R. Optimized Norm-Conserving Vanderbilt Pseudopotentials. *Phys. Rev. B* **2013**, *88*, 085117.

(47) Giannozzi, P.; Andreussi, O.; Brumme, T.; Bunau, O.; Buongiorno Nardelli, M.; Calandra, M.; Car, R.; Cavazzoni, C.; Ceresoli, D.; Cococcioni, M.; et al. Advanced Capabilities for Materials Modelling with Quantum ESPRESSO. *J. Phys.: Condens. Matter* **2017**, *29*, 465901.

(48) Garrity, K. F.; Bennett, J. W.; Rabe, K. M.; Vanderbilt, D. Pseudopotentials for High-Throughput DFT Calculations. *Comput. Mater. Sci.* **2014**, *81*, 446–452.

(49) Perdew, J. P. Density Functional Theory and the Band Gap Problem. *Int. J. Quantum Chem.* **1985**, *28*, 497–523.

(50) Perdew, J. P.; Ernzerhof, M.; Burke, K. Rationale for Mixing Exact Exchange with Density Functional Approximations. *J. Chem. Phys.* **1996**, *105*, 9982–9985.

(51) Adamo, C.; Barone, V. Toward Reliable Density Functional Methods without Adjustable Parameters: The PBE0 Model. *J. Chem. Phys.* **1999**, *110*, 6158–6170.

(52) Chen, W.; Pasquarello, A. Band-Edge Levels in Semiconductors and Insulators: Hybrid Density Functional Theory versus Many-Body Perturbation Theory. *Phys. Rev. B* **2012**, *86*, No. 035134.

(53) Steiner, K.; Chen, W.; Pasquarello, A. Band Offsets of Lattice-Matched Semiconductor Heterojunctions through Hybrid Functionals and G0W0. *Phys. Rev. B* **2014**, *89*, 205309.

(54) Lin, L. Adaptively Compressed Exchange Operator. *J. Chem. Theory Comput.* **2016**, *12*, 2242–2249.

(55) Jocić, M.; Vukmirović, N. Ab Initio Construction of Symmetry-Adapted $k \cdot p$ Hamiltonians for the Electronic Structure of Semiconductors. *Phys. Rev. B* **2020**, *102*, 085121.

(56) Oldag, T.; Aussieker, T.; Keller, H. L.; Preitschaft, C.; Pftzner, A. Solvothermale Synthese Und Bestimmung Der Kristallstrukturen von AgBiI_4 Und Ag_3BiI_6 . *Z. Anorg. Allg. Chem.* **2005**, *631*, 677–682.

(57) Prasad, M. D.; Krishna, M. G.; Batabyal, S. K. Silver Bismuth Iodide Nanomaterials as Lead-Free Perovskite for Visible Light Photodetection. *ACS Appl. Nano Mater.* **2021**, *4*, 1252–1259.

(58) Crovetto, A.; Hajjifarassar, A.; Hansen, O.; Seger, B.; Chorkendorff, I.; Vesborg, P. C. K. Parallel Evaluation of the BiI_3 , BiOI , and Ag_3BiI_6 Layered Photoabsorbers. *Chem. Mater.* **2020**, *32*, 3385–3395.

(59) Sengupta, A.; Mandal, K. C.; Zhang, J. Z. Ultrafast Electronic Relaxation Dynamics in Layered Iodide Semiconductors: A Comparative Study of Colloidal BiI_3 and PbI_2 Nanoparticles. *J. Phys. Chem. B* **2000**, *104*, 9396–9403.

(60) Gaarenstroom, S. W.; Winograd, N. Initial and Final State Effects in the ESCA Spectra of Cadmium and Silver Oxides. *J. Chem. Phys.* **1977**, *67*, 3500–3506.

(61) Khazaei, M.; Sardashti, K.; Chung, C. C.; Sun, J. P.; Zhou, H.; Bergmann, E.; Dunlap-Shohl, W. A.; Han, Q.; Hill, I. G.; Jones, J. L.; et al. Dual-Source Evaporation of Silver Bismuth Iodide Films for Planar Junction Solar Cells. *J. Mater. Chem. A* **2019**, *7*, 2095–2105.

(62) Qiu, W.; Dudder, G. J.; Zhao, X.; Perry, S. S.; Nino, J. C. Interfacial Reactivity of Au, Pd, and Pt on BiI_3 (001): Implications for Electrode Selection. *ACS Appl. Mater. Interfaces* **2011**, *3*, 1910–1917.

(63) Ferfolja, K.; Valant, M.; Mikulska, I.; Gardonio, S.; Fanetti, M. Chemical Instability of an Interface between Silver and Bi_2Se_3 Topological Insulator at Room Temperature. *J. Phys. Chem. C* **2018**, *122*, 9980–9984.

(64) Pignić, M.-C.; Patra, S.; Huart, L.; Milosavljević, A. R.; Renault, J. P.; Leroy, J.; Nicolas, C.; Sublemontier, O.; le Caër, S.; Thill, A. Experimental Determination of the Curvature-Induced Intra-Wall Polarization of Inorganic Nanotubes. *Nanoscale* **2021**, *13*, 19650–19662.

(65) Schürmann, R.; Titov, E.; Ebel, K.; Kogikoski, S.; Mostafa, A.; Saalfrank, P.; Milosavljević, A. R.; Bald, I. The Electronic Structure of the Metal-Organic Interface of Isolated Ligand Coated Gold Nanoparticles. *Nanoscale Adv.* **2022**, *4*, 1599–1607.

(66) Premkumar, S.; Liu, D.; Zhang, Y.; Nataraj, D.; Ramya, S.; Jin, Z.; Mamba, B. B.; Kuvarega, A. T.; Gui, J. Stable Lead-Free Silver Bismuth Iodide Perovskite Quantum Dots for UV Photodetection. *ACS Appl. Nano Mater.* **2020**, *3*, 9141–9150.

(67) Hinuma, Y.; Pizzi, G.; Kumagai, Y.; Oba, F.; Tanaka, I. Band Structure Diagram Paths Based on Crystallography. *Comput. Mater. Sci.* **2017**, *128*, 140–184.

Electronic Properties of Silver-Bismuth Iodide Rudorffite Nanoplatelets

Danijela Danilović^{1,2}, Aleksandar R. Milosavljević^{3*}, Pitambar Sapkota^{4,5}, Radovan Dojčilović^{1,2,6}, Dragana Tošić¹, Nenad Vukmirović⁷, Milan Jocić⁷, Vladimir Djoković^{1,2}, Sylwia Ptasinska^{4,5}, and Dušan K. Božanić^{1,2*}

¹ Department of Radiation Chemistry and Physics, "Vinča" Institute of Nuclear Sciences - National Institute of the Republic of Serbia, University of Belgrade, P.O. Box 522, 11001 Belgrade, Serbia

² Center of Excellence for Photoconversion, Vinča" Institute of Nuclear Sciences - National Institute of the Republic of Serbia, University of Belgrade, P.O. Box 522, 11001 Belgrade, Serbia

³ Synchrotron SOLEIL, l'Orme des Merisiers, St. Aubin, BP48, 91192 Gif sur Yvette Cedex, France

⁴ Radiation Laboratory, University of Notre Dame, Notre Dame, IN 46556, USA

⁵ Department of Physics, University of Notre Dame, Notre Dame, IN 46556, USA

⁶ Department of Experimental and Health Sciences (DCEXS), Pompeu Fabra University (UPF), 08003 Barcelona, Spain

⁷ Institute of Physics Belgrade, University of Belgrade, Pregrevica 118, 11080, Belgrade, Serbia

Corresponding authors: *A.R.M. milosavljevic@synchrotron-soleil.fr; *D.K.B. bozanic@vin.bg.ac.rs

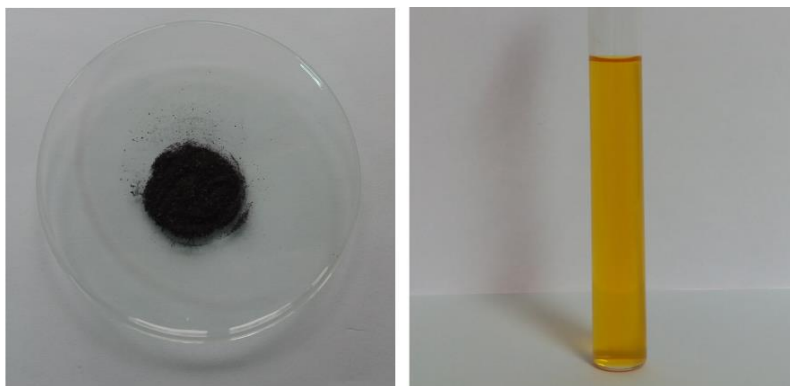


Figure S1. Photographs of Ag-Bi-I powder, and the Ag-Bi-I dispersed in acetonitrile.

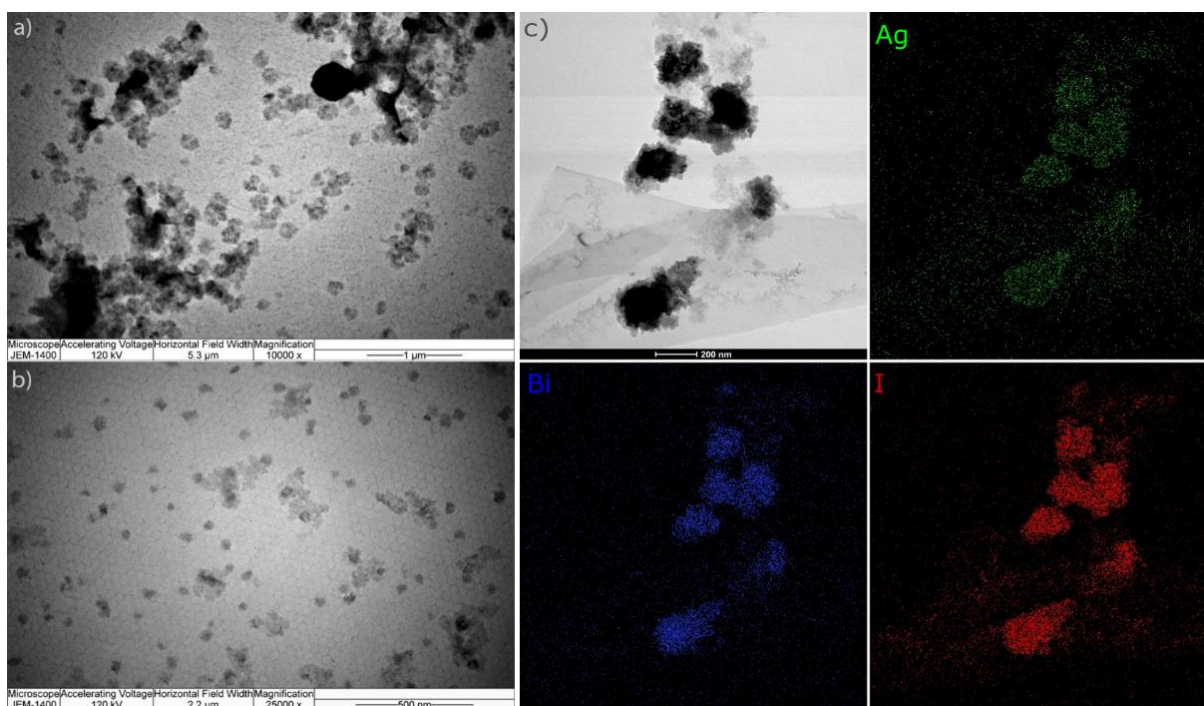


Figure S2. TEM images of a) Ag-Bi-I and b) BiI₃ nanoplatelets and c) HRTEM/EDS mapping of Ag-Bi-I nanoplatelets for silver, bismuth, and iodine.

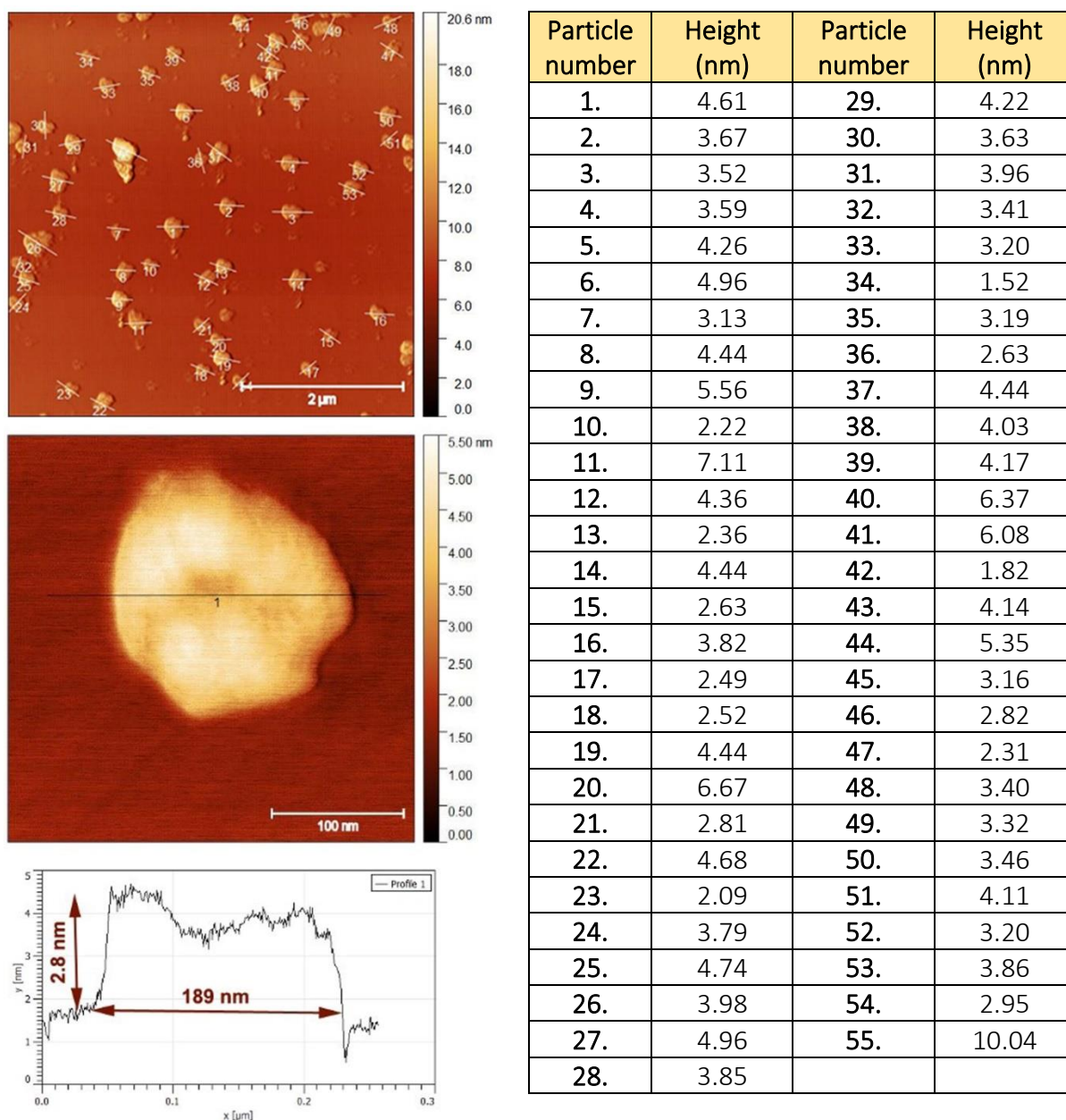


Figure S3. AFM profile analysis procedure for determination of the height distribution of Ag-Bi-I nanoplatelets and the corresponding results table. The height profile in the random direction of the observed particles was evaluated and maximum height was considered as the thickness of the particle.

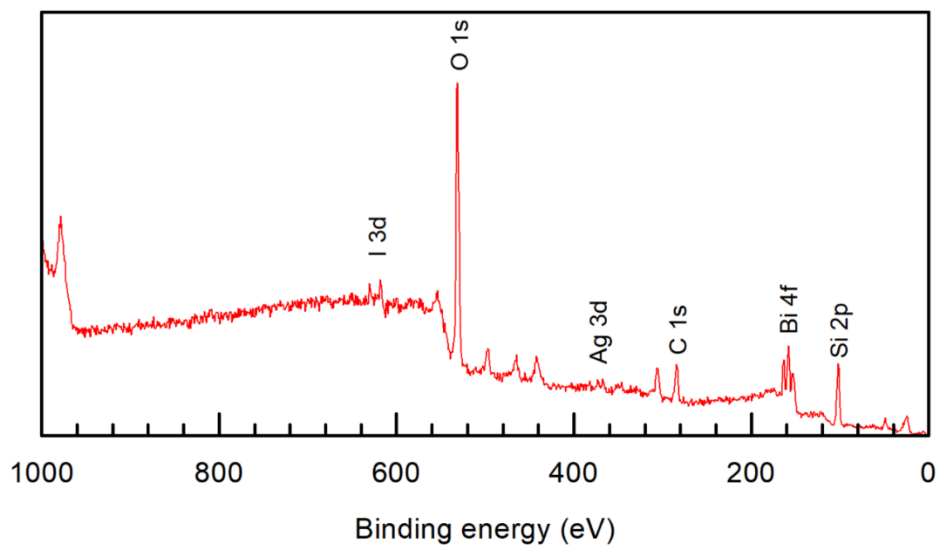


Figure S4. XPS survey scan of Ag-Bi-I nanoplatelets.

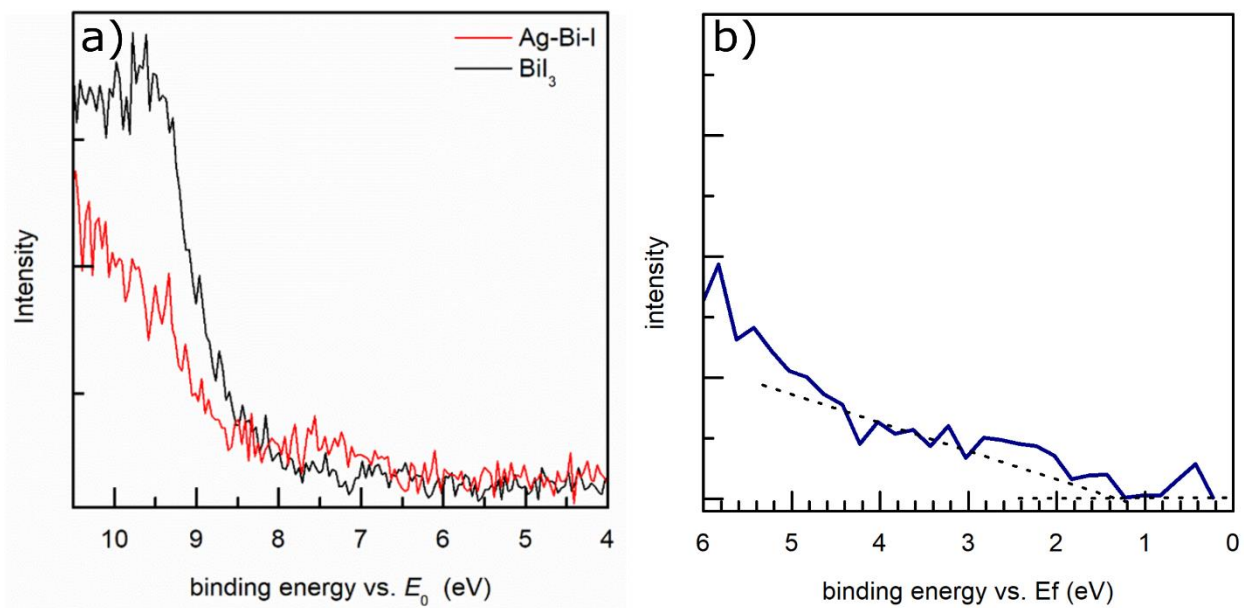


Figure S5. (a) Valence region photoemission spectra of Ag-Bi-I and BiI₃ aerosol particles recorded at 100 eV using XAPS. (b) Valence region photoemission spectrum of Ag-Bi-I measured using XPS at 1486.6 eV.

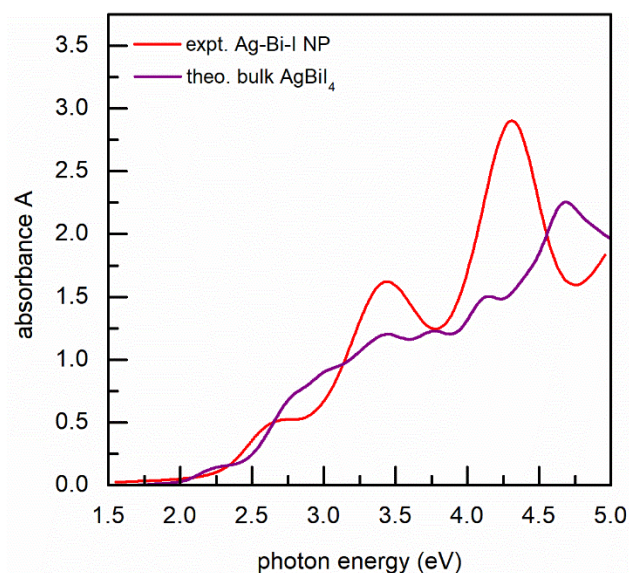


Figure S6. UV-vis absorption spectrum of Ag-Bi-I nanoplatelets dispersed in acetonitrile (red line) and the theoretical absorption of bulk AgBi_4 material (purple line) calculated by the procedure described in Section A8. The theoretical curve was shifted by 0.4 eV to match the theoretical value of the band gap with the experimental one.

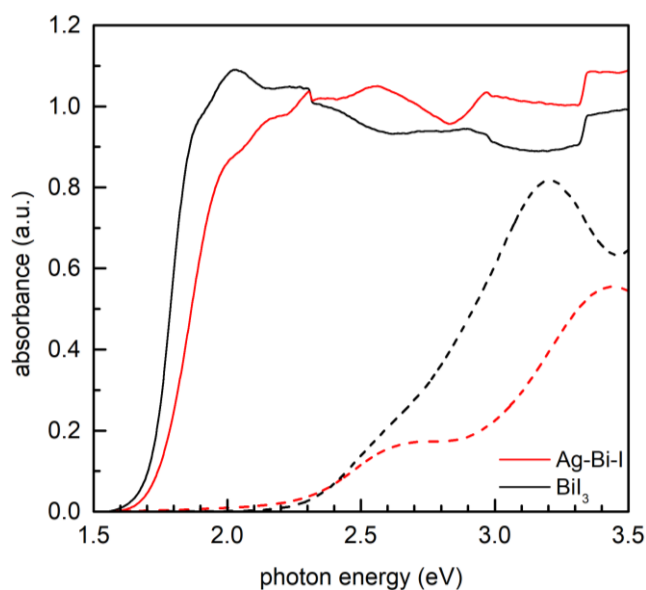


Figure S7. Absorption spectra of Ag-Bi-I and BiI_3 powders (dashed lines) and their colloidal dispersions in acetonitrile (solid lines).

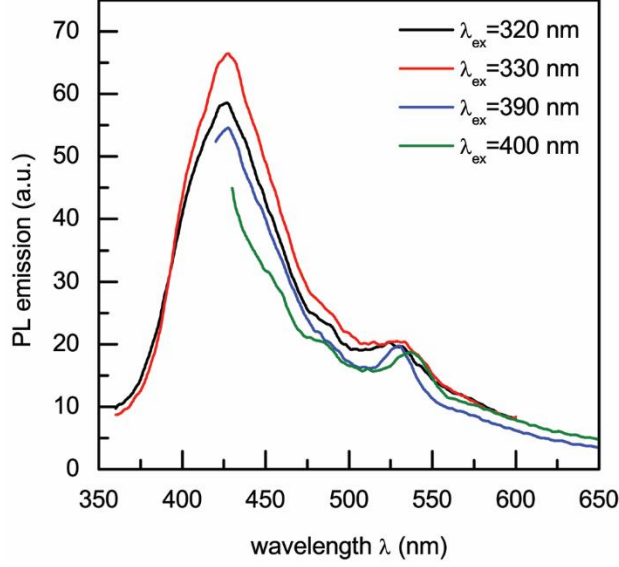


Figure S8. Photoluminescence emission spectra of Ag-Bi-I nanoplatelets dispersed in acetonitrile.

A1 Parametrization of $\mathbf{k} \cdot \mathbf{p}$ Hamiltonian using the data obtained from DFT calculations

To enable accurate calculations of wider quantum wells, we constructed the $\mathbf{k} \cdot \mathbf{p}$ Hamiltonian following the approach of Ref ¹. Namely, the Hamiltonian matrix takes the form

$$H_{mn}(\mathbf{k}) = H_{mn}^{(1)}(\mathbf{k}) + H_{mn}^{(2)}(\mathbf{k}),$$

where

$$H_{mn}^{(1)}(\mathbf{k}) = \left[E_n(\mathbf{k}_0) + \frac{\hbar^2(\mathbf{k} - \mathbf{k}_0)^2}{2m_0} \right] \delta_{mn} + \frac{\hbar(\mathbf{k} - \mathbf{k}_0)}{m_0} \langle \Psi_{n\mathbf{k}_0} | \mathbf{p} | \Psi_{m\mathbf{k}_0} \rangle,$$

$$H_{mn}^{(2)}(\mathbf{k}) = \frac{\hbar^2}{m_0^2} \sum_l \frac{\langle \Psi_{m\mathbf{k}_0} | (\mathbf{k} - \mathbf{k}_0) \cdot \mathbf{p} | \Psi_{l\mathbf{k}_0} \rangle \langle \Psi_{l\mathbf{k}_0} | (\mathbf{k} - \mathbf{k}_0) \cdot \mathbf{p} | \Psi_{n\mathbf{k}_0} \rangle}{[E_n(\mathbf{k}_0) + E_m(\mathbf{k}_0)]/2 - E_l(\mathbf{k}_0)},$$

$E_n(\mathbf{k}_0)$ is the energy of band n at the wave vector \mathbf{k}_0 , $|\Psi_{n\mathbf{k}_0}\rangle$ is the corresponding wave function, and \mathbf{p} is the momentum operator. The indices m and n denote the main bands that are used to construct the $\mathbf{k} \cdot \mathbf{p}$ Hamiltonian, while the index l denotes the remaining bands. The effects of the later bands are included in calculations perturbatively. The $\mathbf{k} \cdot \mathbf{p}$ Hamiltonian is constructed by calculating all the elements of the Hamiltonian matrix starting from calculated energies $E_n(\mathbf{k}_0)$ and wave functions $|\Psi_{n\mathbf{k}_0}\rangle$ of the bulk material. One can use either the energies and wave functions obtained from DFT/PBE calculation, or the ones obtained from the hybrid PBE0 functional calculation. In the latter case, it is expected that band gap of quantum wells would be significantly more accurate. Once the $\mathbf{k} \cdot \mathbf{p}$ Hamiltonian is obtained, the electronic structure of the quantum well can be calculated according to the procedure described in Section III B of Ref ¹.

A2 Model for atomic structure of bulk Ag-Bi-I material

As a model for atomic structure of the Ag-Bi-I material we used the rhombohedral AgBiI₄ material. We constructed its atomic structure as follows. We started with an atomic structure of the rhombohedral CdCl₂, and lattice parameters given in Ref. ² (Table I therein). We replaced Cl atoms with I, while we replaced the Cd atom in one primitive cell with Ag atom and the Cd atom in the neighboring primitive cell with the Bi atom. We then performed DFT/PBE based relaxation of lattice parameters and atomic positions. The final atomic structure that we obtained following this strategy is given in Table S1.

Lattice constants (Å):			
a = 7.028	b = 7.028	c = 7.220	
Lattice angles (degrees):			
alpha = 80.14	beta = 88.86	gamma = 145.50	
Fractional atomic coordinates:			
Ag	0.00000	0.00000	0.00000
Bi	0.50000	0.50000	0.50000
I	0.63580	0.36420	0.88645
I	0.36420	-0.36420	0.11355
I	0.14486	-0.14486	0.37397
I	0.85514	0.14486	0.62603

Table S1. Lattice parameters and atomic coordinates of AgBiI₄ obtained from DFT/PBE calculations.

A3 Model for atomic structure of nanoplatelets

Experimentally investigated nanoplatelets have much larger lateral dimensions than thickness. For this reason, we modeled them as quantum wells that are infinite in *xy*-plane with the thickness *L* in the *z*-direction. To construct the atomic structure of such quantum wells, we performed the following procedure: we first noted that the atomic structure of the rhombohedral AgBiI₄ that we investigated can be constructed by putting together different atomic planes spanned by the vectors **a** + **b** and **c**. One such plane that contains Ag and Bi atoms is sandwiched between two planes that contain I atoms. These three planes form one monolayer of the material. We constructed a quantum well consisting of *n* monolayers by translating one monolayer *n* times by vector **a**. The example of atomic structure of 8 monolayer quantum well is presented in Figure S9.

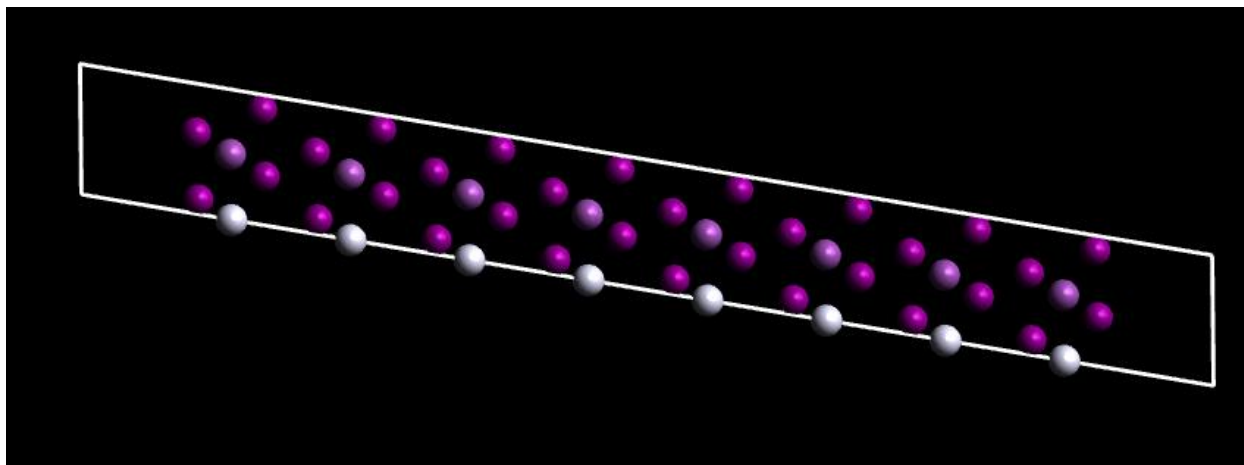


Figure S9. Atomic structure of a quantum well consisting of 8 monolayers. White lines denote the supercell used in the calculation of the electronic structure. Ag atoms are shown in white, Bi atoms are shown in violet, while I atoms are shown in magenta.

To calculate the electronic structure of a quantum well, we applied periodic boundary conditions in the xy -plane, while included a sufficiently thick vacuum layer in the z -direction (see Figure S9) to avoid electronic coupling in the z -direction between atoms from neighboring supercells.

A4 Determination of absolute positions of bulk energy levels with respect to vacuum

Density functional theory calculations with plane-wave basis and periodic boundary conditions do not yield the absolute value of the position of the energy levels with respect to vacuum. To align these levels with vacuum, we calculated the dependence of the averaged potential (the sum of the Hartree potential and the local part of the ionic pseudopotential averaged over the xy -plane) on z -coordinate. The dependence for 8 monolayer quantum well and for bulk is presented in Figure S10. It can be noted that the potential outside the well is flat, but it is different from zero. Therefore, the value of the potential outside the well gives us the shift that is necessary to align all the energy levels in the quantum well calculation with vacuum level. Next, we noticed that the shape of the bulk potential matches the potential in the middle of the well apart from a constant energy shift. By shifting the bulk potential by this energy shift, the bulk potential is then aligned with the quantum well potential. Hence, by aligning the bulk potential with quantum well potential and the quantum well potential with the vacuum level, we eventually aligned the bulk potential with the vacuum level, see Figure S11. Using the mentioned procedure and DFT/PBE calculation method, we found the valence band maximum (VBM) energy to be -5.1 eV.

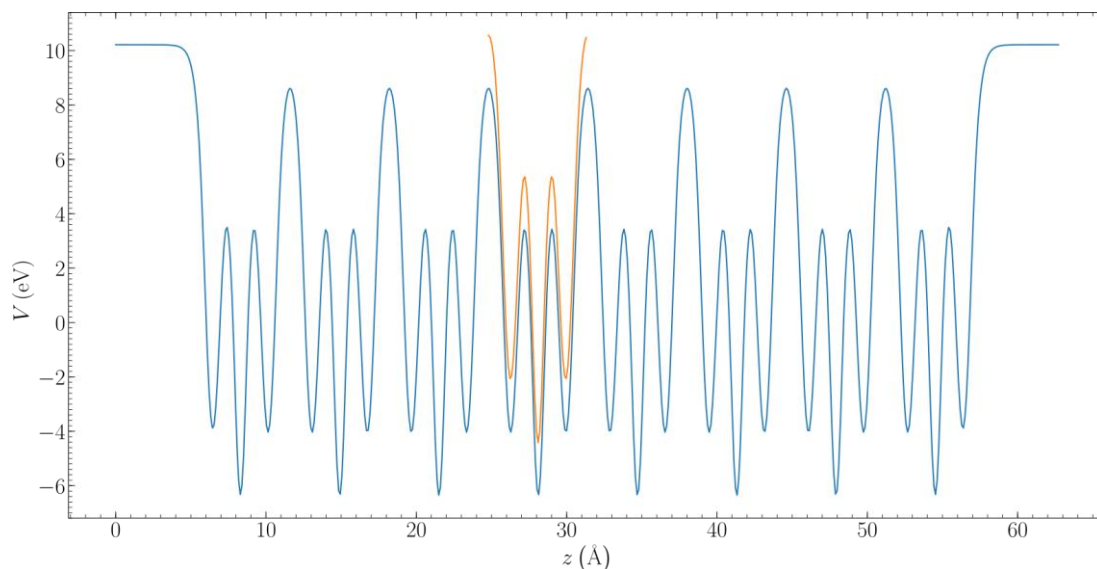


Figure S10. Averaged potential profile as obtained from DFT/PBE calculation of the 8 monolayer quantum well (blue line) and the bulk material (orange line).

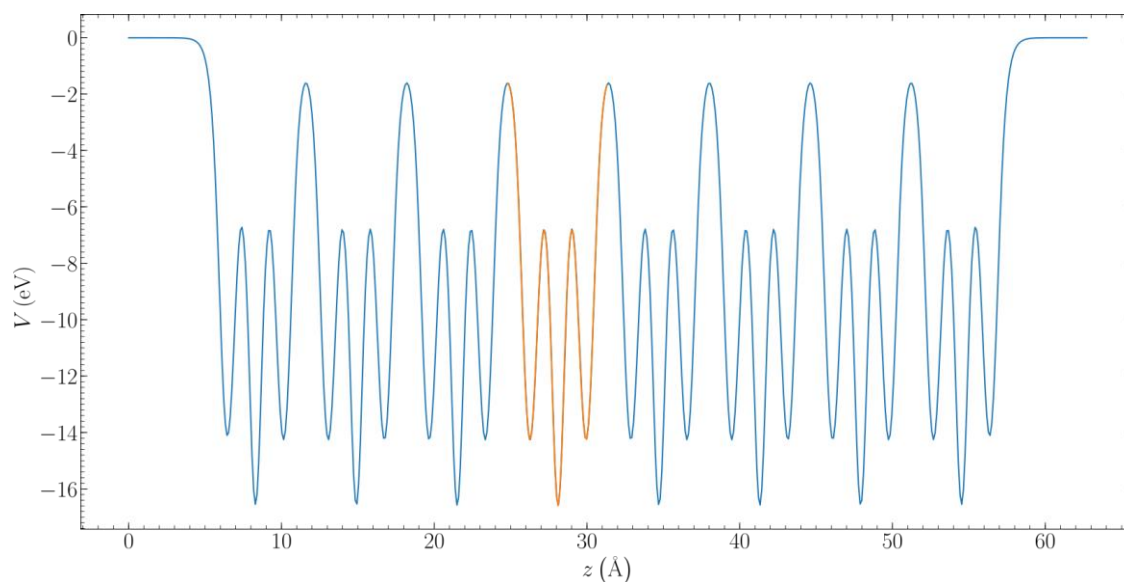


Figure S11. Averaged potential profile of the 8 monolayer quantum well (blue line) and the bulk material (orange line). The potentials obtained from DFT/PBE calculation were shifted to align the quantum well potential with vacuum and the bulk potential with the potential in the middle of the quantum well.

Still, the DFT/PBE calculation method gave slightly lower value for the position of the bulk VBM energy with respect to vacuum level. To improve the calculation procedure, we used the result obtained in hybrid PBE0 functional calculation. The VBM energy value obtained by DFT/PBE method is corrected by taking into account the differences in bulk VBM energies calculated using DFT/PBE0 and DFT/PBE methods. Such an approach is justified, because both PBE and PBE0 calculation methods when applied to the identical bulk material, using the same plane wave

computational code, have a common energy reference. Using this procedure we found VBM energy of the bulk material to be -5.95 eV.

A5 Electronic band structure of quantum wells calculated using DFT/PBE

Electronic structure calculations within DFT/PBE approach were performed for quantum wells that have from one to 8 monolayers. The dependence of quantum well band gap on width is presented in Figure S12. We found that this dependence is rather weak. For example, in the range from 2 to 5 nm the gap changes by about 50 meV indicating that the effects that come from quantum confinement are not particularly significant.

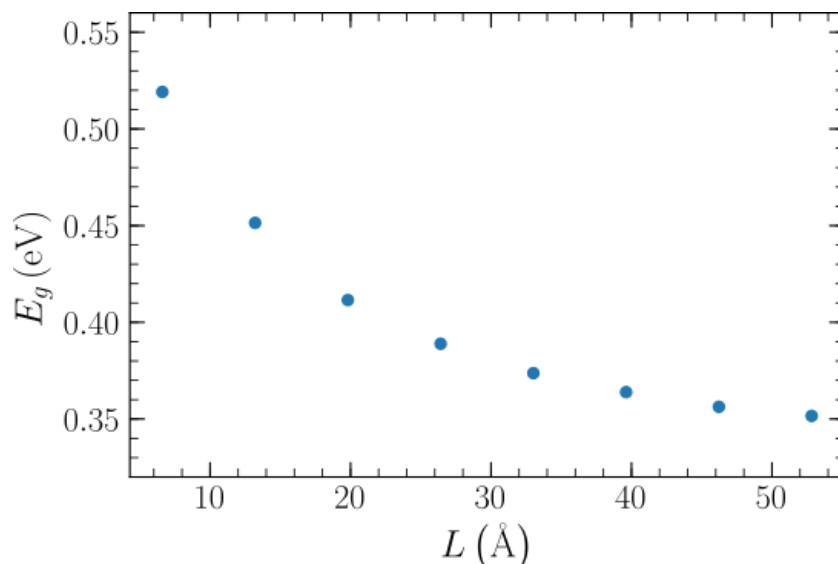


Figure S12. The dependence of quantum well band gap (E_g) on its width(L) calculated by DFT/PBE.

In Figures S13 and S14 we show the electronic band structure of the quantum well along several characteristic directions of the two-dimensional Brillouin zone. The results suggest that the band structure of multilayered quantum wells is rather similar to the band structure of one monolayer quantum well. It can be seen in Figure S14 that each band in Figure S13 is transformed into six similar and closely spaced bands. This also implies that the coupling between different monolayers of the material is rather weak. Consequently, the electronic structure of a single monolayer represents fairly well the electronic structure of the multilayered or even the bulk material. For this reason, the band gap should not be affected by the change in the thickness of the particles (number of quantum wells in the stack), which the results in Figure S12 indeed show.

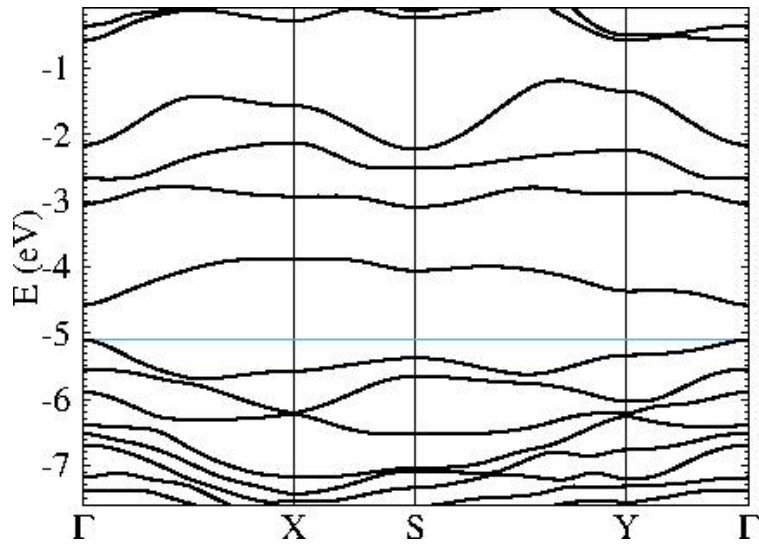


Figure S13. Electronic structure of single monolayer quantum well calculated using DFT/PBE. The blue horizontal line represents the valence band maximum energy. The energies are given with respect to the vacuum level.

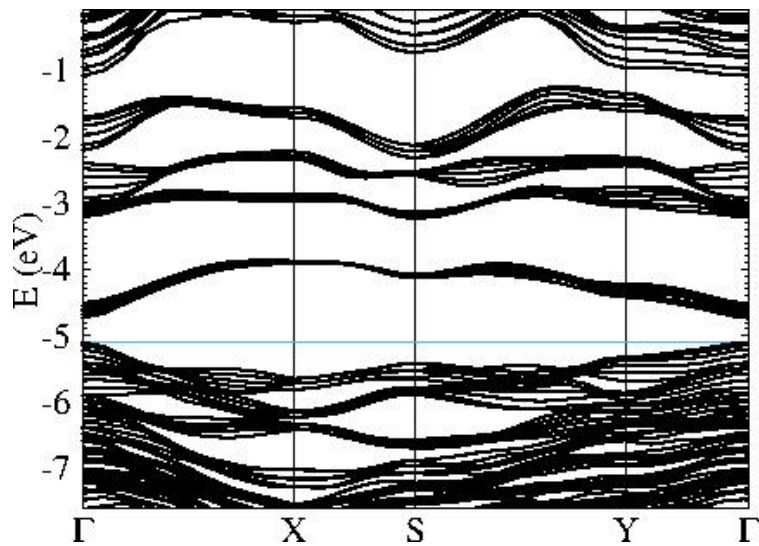


Figure S14. Electronic structure of six-layer stack of quantum wells calculated using DFT/PBE. The blue horizontal line represents the valence band maximum energy. The energies are given with respect to the vacuum level.

A6 Electronic states of quantum wells calculated using the $\mathbf{k} \cdot \mathbf{p}$ method parameterized by using results from DFT/PBE calculations

We calculated the electronic states at the top of the valence band and the bottom of the conduction band of the quantum wells using a 4-band $\mathbf{k} \cdot \mathbf{p}$ Hamiltonian. The Hamiltonian was derived from two highest (degenerate) states in the bulk valence band and two lowest (degenerate) states in the bulk conduction band at the Y_2 point where these bulk bands exhibit their maximum and minimum.

To check the accuracy of the $\mathbf{k} \cdot \mathbf{p}$ method, the calculation was first performed using the Hamiltonian derived from energies and wave functions obtained from DFT/PBE calculation. In this case, the $\mathbf{k} \cdot \mathbf{p}$ results can be compared to the results obtained from full DFT/PBE calculation of quantum wells. This comparison is presented in Figure S15. An excellent agreement between DFT/PBE and $\mathbf{k} \cdot \mathbf{p}$ results was found except for thinnest wells where $\mathbf{k} \cdot \mathbf{p}$ is not expected to perform well.

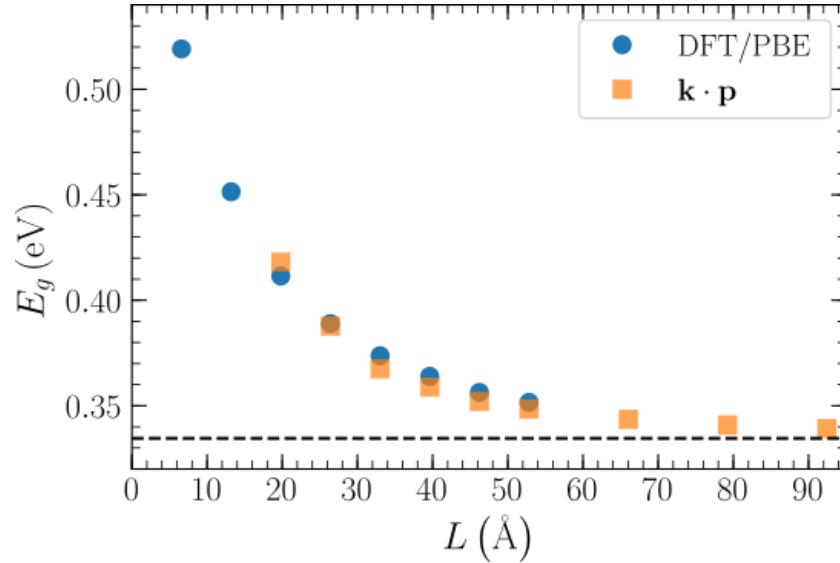


Figure S15. Dependence of quantum well band gap on its width calculated using DFT/PBE and using the $\mathbf{k} \cdot \mathbf{p}$ method with Hamiltonian parameterized with data from DFT/PBE calculations.

A7 Dielectric contrast effect

We also estimated the effect of dielectric contrast between the well and the surroundings. Self-energy arising from this effect was calculated using Eq. (4) from Ref. ³. Assuming the high frequency dielectric constants of 2.1 for AgBiI_4 ⁴ and 1.8 for acetonitrile, we obtained that the change of energy levels is of the order of 25 meV for 2 nm wide quantum wells and decreases as the well width increases.

A8 Absorption spectrum of bulk AgBiI_4 material

To understand the measured absorption spectrum, we performed the calculation of the absorption of bulk AgBiI_4 material. We have previously observed (Figure 7 in the main part of the paper) that the quantum confinement effects are weak. Therefore, it is expected that the absorption spectrum of quantum well and the absorption spectrum of bulk should be similar.

The absorption coefficient is proportional to the quantity

$$A(E) = \frac{1}{N_k} \sum_{\mathbf{k}} \sum_{v,c} \frac{1}{3} \left[|p_x^{vc}(\mathbf{k})|^2 + |p_y^{vc}(\mathbf{k})|^2 + |p_z^{vc}(\mathbf{k})|^2 \right] \frac{\delta[E_c(\mathbf{k}) - E_v(\mathbf{k}) - E]}{E_c(\mathbf{k}) - E_v(\mathbf{k})}.$$

In this equation, the sum is performed over N_k points from the first Brillouin zone and over all valence bands v and conduction bands, c . $E_c(\mathbf{k})$ and $E_v(\mathbf{k})$ denote the energies of states involved in the transition, while $\mathbf{p}^{vc}(\mathbf{k}) = \langle \Psi_{v\mathbf{k}} | \mathbf{p} | \Psi_{c\mathbf{k}} \rangle$ are the momentum matrix elements

between these states. In actual calculation procedure, the delta function was replaced by a Gaussian with standard deviation of 100 meV.

To perform the calculation on a sufficiently dense grid of \mathbf{k} points, we performed $\mathbf{k} \cdot \mathbf{p}$ interpolation of energies and wave functions. First, we carried out a hybrid PBE0 functional calculation on a $4 \times 4 \times 4$ grid of points in reciprocal space. Then, for each \mathbf{k} point which is not on that grid, we found the point \mathbf{k}_0 from the grid closest to that point and construct the $\mathbf{k} \cdot \mathbf{p}$ Hamiltonian with \mathbf{k}_0 as the reference point. By solving the eigenvalue problem of that Hamiltonian, we obtained the energies, wave functions, and momentum matrix elements at \mathbf{k} .

The absorption spectra calculated by mentioned procedure is shown in Figure S16. Each of the absorption curves is calculated using different sizes of the \mathbf{k} point grid. As can be seen, the curves converge starting from $8 \times 8 \times 8$ grid. The calculated spectrum clearly shows a rise in absorbance as energy increases, the trend that is observed experimentally. Also, the spectrum calculated on a $8 \times 8 \times 8$ grid exhibits a peak at 4.4 eV which matches well the experimental peak at 4.3 eV. The experimental absorption onset at 2.2 eV is larger than the energy onset obtained by calculations. Also, the experimental absorption peaks at 2.71 and 3.44 eV cannot be clearly distinguished in the calculated spectrum.

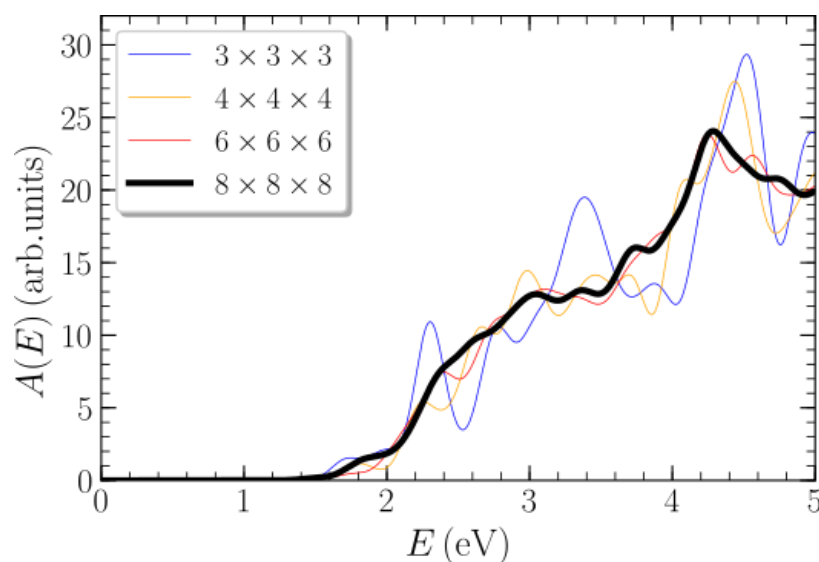


Figure S16. Absorption spectra of bulk AgBiI₄ material. The presented results correspond to different sizes of the \mathbf{k} point grid.

References

- (1) Jocić, M.; Vukmirović, N. Ab Initio Construction of Symmetry-Adapted $\mathbf{k} \cdot \mathbf{p}$ Hamiltonians for the Electronic Structure of Semiconductors. *Phys. Rev. B* **2020**, *102*, 085121.
- (2) Koedtrud, A.; Goto, M.; Amano Patino, M.; Tan, Z.; Guo, H.; Nakamura, T.; Handa, T.; Chen, W. T.; Chuang, Y. C.; Sheu, H. S.; et al. Structure-Property Relations in Ag-Bi-I Compounds: Potential Pb-Free Absorbers in Solar Cells. *J. Mater. Chem. A* **2019**, *7*, 5583–5588.

- (3) Cho, Y.; Berkelbach, T. C. Environmentally Sensitive Theory of Electronic and Optical Transitions in Atomically Thin Semiconductors. *Phys. Rev. B* **2018**, *97*, 041409.
- (4) Hosseini, S. S.; Adelifard, M.; Ataei, M. An Investigation on Physical Properties of Ag₂BiI₅ Absorber Layers Synthesized by Microwave Assisted Spin Coating Technique. *J. Mater. Sci.: Mater. Electron.* **2019**, *30*, 5021–5029.